Banner appropriate to article type will appear here in typeset article

Mode selection in concentric jets: the steady-steady 1:2 resonant mode interaction with O(2) symmetry

A. Corrochano [1], J. Sierra-Ausín[2,3], J. A. Martin[1], D. Fabre[2], S. Le Clainche[1] †

[1]School of Aerospace Engineering, Universidad Politécnica de Madrid, Madrid 28040, Spain

[2]Institut de Mécanique des Fluides de Toulouse (IMFT), Toulouse 31400, France

[3] DIIN, Universit´a degli Studi di Salerno, Via Giovanni Paolo II, 84084 Fisciano (SA), Italy

(Received xx; revised xx; accepted xx)

The linear and non-linear stability of two concentric jets separated by a duct wall is analysed by means of global linear stability and weakly non-linear analysis. Three governing parameters are considered, the Reynolds number based on the inner jet, the inner-to-outer jet velocity ratio (δ_u), and the length of the duct wall (L) separating the jet streams. Global linear stability analysis demonstrates the existence of unsteady modes of inherent convective nature, and symmetry-breaking modes that lead to a new non-axisymmetric steady-state with a single or double helix. Additionally, we highlight the existence of multiple steady-states, as a result of a series of saddle-node bifurcations and its connection to the changes in the topology of the flow. The neutral lines of stability have been computed for inner-to-outer velocity ratios within the range $0 < \delta_u < 2$ and duct wall distances in the interval $0.5 < L < 4$. They reveal the existence of hysteresis, and mode switching between two symmetry breaking modes with azimuthal wavenumbers $1 : 2$. Finally, the mode interaction is analysed, highlighting the presence of travelling waves emerging from the resonant interaction of the two steady states, and the existence of robust heteroclinic cycles that are asymptotically stable.

Key words: Concentric jets, linear stability analysis, dynamical systems, wakes/jets

1. Introduction

Double concentric jets is a configuration enhancing the turbulent mixing of two jets, which is used in several industrial applications where the breakup of the jet into droplets due to flow instabilities is presented as the key technology. Combustion (i.e., combustion chamber of rocket engines, gas turbine combustion, internal combustion engines, etc.) and noise reduction (e.g., in turbofan engines) are the two main applications of this geometry, although the annular jets can also be found in some other relevant applications such as ink-jet printers or spray coating.

The qualitative picture emerging from this type of flow divides the inner field of concentric jets in three different regions: (i) initial merging zone, (ii) transitional zone and (iii) merged

† Email address for correspondence: soledad.leclainche@upm.es

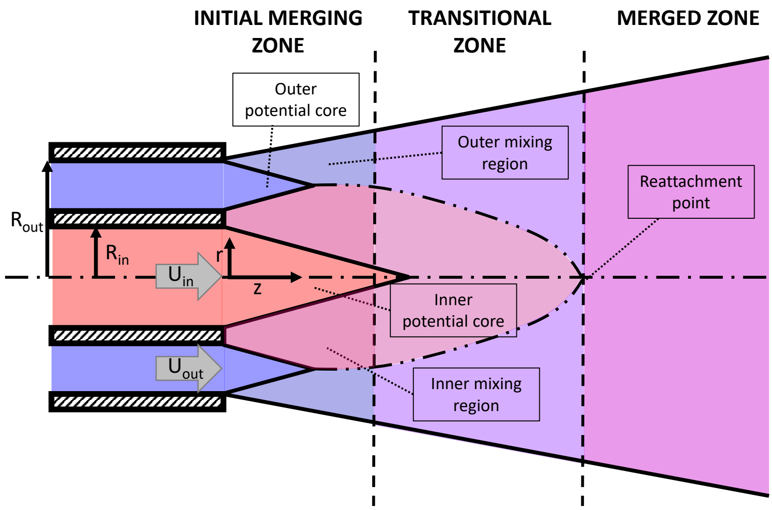

Figure 1: Sketch representing the three flow regimes in the near field of double concentric jets. Figure based on the sketch presented in (Ko & Kwan 1976; Talamelli & Gavarini 2006).

zone, as presented in fig. 1, that follows the initial sketch presented by Ko & Kwan (1976). In the initial merging zone (i), just at the exit of the two jets, two axisymmetric shear layers (inner and outer boundary layer) develop and start to merge. In this region, we distinguish the inner and outer shear layers, related with the inner and outer jet stream. Then, most of the mixing occurs in the transitional zone (ii), that extends until the external shear layer reaches the centreline. Finally, in the merged zone (iii), the two jets are totally merged, modelling a single jet flow.

Several parameters define the characteristic of this flow: the inner and outer jet velocities, the jet diameters, the shape and thickness of the wall separating both jets, the Reynolds number, the boundary layer state and thickness at the jet exit and the free stream turbulence. Based on these parameters, it is possible to identify several types of flow behaviour, which can be related with the presence of flow instabilities.

Numerous studies have investigated the interaction between the inner and outer shear layers of the jet and their effect on the flow instability. Starting with Ko & Kwan (1976), they postulated that the double concentric jet configuration could be considered as a combination of single jets. Nevertheless, Dahm *et al.* (1992) revealed by means of flow visualisations, diverse topology patterns as function of the outer/inner jet velocity ratio, reflecting that the dynamics of the inner and outer jet shear layers were different from that in a single jet. Moreover, this study exhibited a complex interaction between vortices identified in both shear layers, affecting the instability mechanism of the flow. Subsequently, different flow regimes are recognised as a function of the outer/inner velocity ratio. For cases in which the outer velocity is much larger than the inner velocity, the outer shear layer dominates the flow dynamics (Buresti *et al.* 1994), and a low frequency recirculation bubble can be spotted at the jet outlet (Rehab *et al.* 1997). For still high outer/inner velocity ratios, the outer jet drives the flow dynamics, exciting the inner jet which ends oscillating at the same frequency as the external jet. This trend is known as the lock-in phenomenon, identified by several authors (Dahm *et al.* 1992; Rehab *et al.* 1997; da Silva *et al.* 2003; Segalini & Talamelli 2011). Moreover, the oscillation frequency detected was similar to the one defined by a Kelvin-Helmholtz flow instability, generally encountered in single jets. When the outer/inner velocity ratio is similar, a Von Kármán vortex street is detected near the separating wall, depicted in various investigations (Olsen & Karchmer 1976; Dahm *et al.* 1992; Buresti *et al.* 1994; Segalini & Talamelli 2011). A wake instability affected the inner and outer shear layers, reversing the lock-in phenomenon. Finally, for small outer/inner velocity ratios, the inner jet presents its own flow instability in the shear layer, while a different flow instability was identified in the outer jet, as shown by Segalini & Talamelli (2011).

The velocity ratio between jets has also an influence on noise attenuation, which was analysed experimentally by Williams *et al.* (1969). It was observed that for some given configurations, more noise attenuation was present than for the others, with a maximum between 12 and $15dB$.

Regarding the geometric configuration of the concentric jets, Buresti *et al.* (1994) detected the presence of an alternate vortex shedding when the separation wall thickness between the two jets was sufficiently large, also recognised by Dahm *et al.* (1992); Olsen & Karchmer (1976). This finding was as well presented by Wallace & Redekopp (1992), including the influence of the wall thickness and sharpness on the characteristics of the jet.

This vortex shedding has been theoretically analysed (Talamelli & Gavarini 2006) by means of linear stability analysis, and experimentally tested (Örlü *et al.* 2008). These investigations agree on the vortex shedding driving the evolution of both outer and inner shear layer. Consequently, a global absolute instability can be triggered by this mechanism with no external energy input. The vortex shedding can be therefore considered as a potential tool for passive flow control, delaying the transition to turbulence by means of controlling the near field of the jet.

The study performed in Talamelli & Gavarini (2006) constituted an entry point for subsequent researches (although ignoring the effect of the duct wall separating the two streams). A similar procedure was employed to investigated the local linear spatial stability of compressible, inviscid coaxial jets (Perrault-Joncas & Maslowe 2008) and lately accounting for the effects of heat conduction and viscosity (Gloor *et al.* 2013). Both investigations found two modes of instability, one being associated with the primary and the other with the secondary stream, showing an independence between modes, the effect of velocity ratio mainly affects the first mode, while the second mode was primarily influenced by the diameter ratio between jets. Gloor *et al.* (2013) also identified parameter regimes in which the stability of the two layers is not independent anymore, and pointed that viscous effects are essential only below a specific Reynolds number. Subsequently, this work was expanded in Balestra *et al.* (2015) to investigate the local inviscid spatio-temporal instability characteristics of heated coaxial jet flows, where the presence of an absolutely unstable outer mode was identified.

Recently, Canton *et al.* (2017) performed a global linear stability analysis to study more in detail this vortex shedding mechanism behind the wall. They examined a concentric jet configuration with a very small wall thickness ($0.1D$, with D the inner jet diameter), but the authors selected an outer/inner velocity ratios where it was known that the alternate vortex shedding behind the wall was driving the flow. A global unstable mode (absolute instability) with azimuthal wavenumber $m = 0$ was found, confirming that the primary instability was axisymmetric (the modes with $m = 1, 2$ were stable at the flow conditions at which the study was carried out). The highest intensity of the global mode was located in the wake of the jet, composed by an array of counter-rotating vortex rings. The shape of the mode changes when moving along its neutral curve, revealing through the numerical simulations a Kelvin-Helmholtz instability over the shear-layer between the two jets and in the outer jet at high Reynolds numbers. Nevertheless, the authors showed that the wavemaker was located in the bubble formed upstream the separating wall, in good agreement with the results presented by Tammisola (2012), who performed a similar stability analysis in a two-dimensional configuration (wakes with co-flow).

The stability of annular jets, a limit case where the inner jets have zero velocity, has also been investigated. In different analyses of annular jets (Bogulawski & Wawrzak 2020; Michalke 1999), it has been illustrated that this type of axisymmetric configuration does not behave as it appears. The $m = 0$ modes studied have been shown to be stable, and the dominant mode found by both studies is helical ($m = 1$). In addition, to characterise the annular jet, these investigations analyse the behaviour of the case by adding an azimuthal component to the inflow velocity, making the discharge of the annular jet eddy-like, comparing the evolution of the frequency and growth rate of this $m = 1$ mode.

The convective stability of weakly swirling coaxial jets has also been studied, as done in Montagnani & Auteri (2019), where the optimal response modes are determined from an external forcing. The impact of velocity ratio between jets, effect of swirl, and influence of Reynolds number is presented by means of non-modal analysis. They showed that small transient perturbations rapidly grow, experiencing a considerable spatial amplification, where nonlinear interactions come into play being capable of triggering turbulence and large oscillations. For non-swirling coaxial jets, the stability characteristics are found to be dominated by the axisymmetric and sinuous optimal modes.

The current study aims to expand the investigations of Canton *et al.* (2017), who used a specific geometry and varied the outer-to-inner velocity ratio. Herein, we aim to provide a complete characterisation of the leading global modes, and to demonstrate the effect of three parameters on the linear stability properties. These three parameters are: the duct wall thickness separating the two jets, which is explored in the interval $L \in [0.5, 4]$, the inner-to-outer velocity δ_u, within the range $\delta_u \in [0, 2]$, and the Reynolds numbers based on the inner jet. We find unstable global modes with azimuthal wavenumbers $m = 0$ (axisymmetric modes), $m = 1$ and $m = 2$.

This work also performs a study of the mode interaction between two steady modes with azimuthal wavenumbers $m = 1$ and $m = 2$. Different analyses have been done to determine the attracting coherent structures when there is an interaction between modes. Some of these flow structures are non-axisymmetric steady states, travelling waves or most remarkably robust heteroclinic cycles.

The article is organised as follows. Section 2 defines the problem and the governing equations for the coaxial jet configuration, as well as the linear stability equations and the methodology for mode selection. A characterisation of the axisymmetric steady-state is done in Section 3. In particular, we show the existence of multiple steady-states, as a result of a series of saddle-node bifurcations. Section 4 is devoted to the discussion of the global linear stability results. Section 4.1 is intended to illustrate the basic features of the most unstable global modes, such as their spatial distribution and frequency content, as well as, a brief discussion about the instability physical mechanism. In the following subsections, we perform a parametric exploration in terms of the inner-to-outer velocity ratio, and the duct wall length between the jet streams in order to determine the neutral curves of global stability. Section 5 undertakes a detailed study of the unfolding of the codimension-two bifurcation between two steady-modes with azimuthal wavenumbers $m = 1$ and $m = 2$. Therein, we discuss the consequences of $1 : 2$ resonance, which leads to the emergence of unsteady flow structures, such as travelling waves or robust heteroclinic cycles, among others. Finally, Section 6 summarises the main conclusions of the current study.

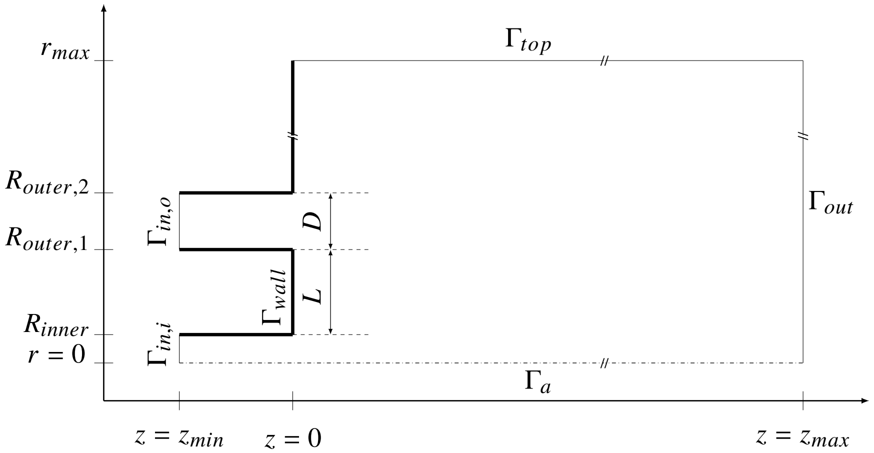

Figure 2: Computational domain of the configuration of two concentric jets, used in StabFem.

2. Problem formulation

2.1. *Computational domain and general equations*

The computational domain, represented in fig. 2, models a coaxial flow configuration, which is composed of two inlet regions, an inner and outer pipe, both having a distance D between walls and length $5D$, i.e. $z_{min} = -5D$. The computational domain has an extension of $z_{max} = 50D$ and $r_{max} = 25D$. The distance between the pipes is equal to L, measured from the inner face of the outer tube to the face of the inner jet.

The governing equations of the flow within the domain are the incompressible Navier–Stokes equations. These are written in cylindrical coordinates (r, θ, z), which are made dimensionless by considering D as the reference length scale and $W_{o,max}$ as the reference velocity scale, which is the maximum velocity in the outer pipe at $z = z_{min}$.

$$\frac{\partial \mathbf{U}}{\partial t} + \mathbf{U}\cdot\nabla\mathbf{U} = -\nabla P + \nabla\cdot\tau(\mathbf{U}), \qquad \nabla\cdot\mathbf{U} = 0, \tag{2.1a}$$

$$\text{with } \tau(\mathbf{U}) = \frac{1}{Re}(\nabla\mathbf{U} + \nabla\mathbf{U}^T), \qquad Re = \frac{W_{o,max}D}{\nu}. \tag{2.1b}$$

The dimensionless velocity vector $\mathbf{U} = (U, V, W)$ is composed of the radial, azimuthal and axial components, P is the dimensionless-reduced pressure, the dynamic viscosity ν and the viscous stress tensor $\tau(\mathbf{U})$.

The incompressible Navier–Stokes equations eq. (2.1) are complemented with the following boundary conditions

$$\mathbf{U} = (0, 0, W_i) \text{ on } \Gamma_{in,i} \text{ and } \mathbf{U} = (0, 0, W_o) \text{ on } \Gamma_{in,o}, \tag{2.2}$$

where

$$W_i = \delta_u \tanh\left(b_i(1-2r)\right) \text{ and } W_o = \tanh\left[b_o\left(1 - \left|\frac{2r - (R_{outer,1} + R_{outer,2})}{D}\right|\right)\right].$$

The parameter δ_u corresponds to the velocity ratio between the two jets, defined as $\delta_u = W_{i,max}/W_{o,max}$, the volumetric flow rate of the inner and outer jet are defined as $\dot{V}_i = 2\pi\int_0^{R_{inner}} rW_i\mathrm{d}r$ and $\dot{V}_o = 2\pi\int_{R_{outer,1}}^{R_{outer,2}} rW_o\mathrm{d}r$, respectively. The parameters b_o and b_i represent the boundary layer thickness within the nozzle, which are fixed equal to 5 (as in

Canton *et al.* (2017)). With this choice of parameters the volumetric flow rate of the inner jet is a function of the inner-to-outer velocity $\dot{V}_i = 3.73\delta_u$, whereas the flow rate of the outer jet is a function of the duct wall length separating the two jets $\dot{V}_o = 5.41L$. There is a weak influence of the boundary layer thickness on the stability properties of the jet, and it is related to the vortex shedding regime developed upstream the separation wall (more details may be found in Talamelli & Gavarini (2006)). Finally, no-slip boundary condition is set on Γ_{wall} and stress-free ($\left(\frac{1}{Re}\tau(\mathbf{U}) - P\right) \cdot \mathbf{n} = \mathbf{0}$) boundary condition is set on Γ_{top} and Γ_{out}, as shown in fig. 2.

In the sequel, Navier–Stokes equations eq. (2.1) and the associated boundary conditions will be written symbolically under the form

$$\mathbf{B}\frac{\partial \mathbf{Q}}{\partial t} = \mathbf{F}(\mathbf{Q}, \boldsymbol{\eta}) \equiv \mathbf{L}\mathbf{Q} + \mathbf{N}(\mathbf{Q}, \mathbf{Q}) + \mathbf{G}(\mathbf{Q}, \boldsymbol{\eta}), \tag{2.3}$$

with the flow state vector $\mathbf{Q} = [\mathbf{U}, P]^T$, $\boldsymbol{\eta} = [Re, \delta_u]^T$, and the entries of the matrix $\mathbf{B}$ arises from rearranging eq. (2.1). Such a form of the governing equations takes into account a linear dependency on the state variable $\mathbf{Q}$ through $\mathbf{L}$. And a quadratic dependency on the parameters and the state variable through operators $\mathbf{G}(\cdot, \cdot)$ and $\mathbf{N}(\cdot, \cdot)$.

2.2. *Asymptotic stability*

2.2.1. *Linear stability analysis*

In this study, the authors attempt to characterise the stable asymptotic state from the spectral properties of the Navier–Stokes equations eq. (2.1). First, let us consider the stability of an axisymmetric steady-state solution named $\mathbf{Q}_0$, which will be also referred to as *trivial steady-state*. For that purpose, let us evaluate a solution of eq. (2.1) in the neighbourhood of the trivial steady state, i.e., a perturbed state as follows,

$$\mathbf{Q}(\mathbf{x}, t) = \mathbf{Q}_0(\mathbf{x}, t) + \varepsilon\hat{\mathbf{q}}(r, z)\mathrm{e}^{-\mathrm{i}(\omega t - m\theta)}, \tag{2.4}$$

where $\varepsilon \ll 1$, $\hat{\mathbf{q}} = [\hat{\mathbf{u}}, \hat{p}]^T$ is the perturbed state, ω is the complex frequnecy and m is the azimuthal wavenumber. The next step consists in the characterisation of the dynamics of small-amplitude perturbations around this base flow by expanding them over the basis of linear eigenmodes (2.4). If there is a pair $[\mathrm{i}\omega_\ell, \hat{\mathbf{q}}_\ell]$ with $\mathrm{Im}(\omega_\ell) > 0$ (resp. the spectrum is contained in the half of the complex plane with negative real part) there exists a basin of attraction in the phase space where the trivial steady-state $\mathbf{Q}_0$ is unstable (resp. stable) (Kapitula & Promislow 2013). The eigenpair $[\mathrm{i}\omega_\ell, \hat{\mathbf{q}}_\ell]$ is determined as a solution of the following eigenvalue problem,

$$\mathbf{J}_{(\omega_\ell, m_\ell)}\hat{\mathbf{q}}_{(z_\ell)} \equiv \left(i\omega_\ell\mathbf{B} - \frac{\partial \mathbf{F}}{\partial \mathbf{q}}|_{\mathbf{q}=\mathbf{Q}_0, \boldsymbol{\eta}=\mathbf{0}}\right)\hat{\mathbf{q}}_{(z_\ell)} = 0, \tag{2.5}$$

where the linear operator $\mathbf{J}$ is the Jacobian of eq. (2.1), and $\left(\frac{\partial \mathbf{F}}{\partial \mathbf{q}}|_{\mathbf{q}=\mathbf{Q}_0, \boldsymbol{\eta}=\mathbf{0}}\right)\hat{\mathbf{q}}_{(z_\ell)} = \mathbf{L}_{m_\ell}\hat{\mathbf{q}}_{(z_\ell)} + \mathbf{N}_{m_\ell}(\mathbf{Q}_0, \hat{\mathbf{q}}_{(z_\ell)}) + \mathbf{N}_{m_\ell}(\hat{\mathbf{q}}_{(z_\ell)}, \mathbf{Q}_0)$. The subscript m_ℓ indicates the azimuthal wavenumber used for the evaluation of the operator. In the following, we account for eigenmodes $\hat{\mathbf{q}}_{(z_\ell)}(r, z)$ that have been normalised in such a way $\langle \hat{\mathbf{u}}_{(z_\ell)}, \hat{\mathbf{u}}_{(z_\ell)} \rangle_{L^2} = 1$.
The identification of the *core* region of the self-excited instability mechanism (Gianneti & Luchini 2007) is evaluated by means of the structural sensitivity tensor

$$\mathbf{S}_s = \left(\hat{\mathbf{u}}^\dagger\right)^* \otimes \hat{\mathbf{u}}. \tag{2.6}$$

2.2.2. *Methodology for the study of mode selection*

In the following, we briefly outline the main aspects of the methodology employed in the study of *mode interaction* or unfolding of a bifurcation with codimension-two, a comprehensive explanation is left to appendix A. Herein, we use the concept of mode interaction as a synonym of the analysis of a bifurcation with codimension-two, that is, a bifurcation satisfying two conditions, e.g., a bifurcation where two modes become at the same time unstable. The determination of the attractor or coherent structure is explored within the framework of equivariant bifurcation theory. The trivial steady-state is axisymmetric, i.e. the symmetry group is the orthogonal group $O(2)$. Near the onset of the instability, dynamics can be reduced to those of the centre manifold. Particularly, due to the non-uniqueness of the manifold one can always look for its simplest polynomial expression, which is known as the *normal form* of the bifurcation. The reduction to the normal form is carried out via a multiple scales expansion of the solution $\mathbf{Q}$ of eq. (2.3). The expansion considers a two scale development of the original time $t \mapsto t + \varepsilon^2\tau$, here ε is the order of magnitude of the flow disturbances, assumed to be small $\varepsilon \ll 1$. In this study we carry out a normal form reduction via a weakly non-linear expansion, where the small parameters are

$$\varepsilon^2_{\delta_u} = \delta_{u,c} - \delta_u \sim \varepsilon^2 \text{ and } \varepsilon^2_\nu = (\nu_c - \nu) = \left(Re_c^{-1} - Re^{-1}\right) \sim \varepsilon^2.$$

A fast timescale t of the self-sustained instability and a slow timescale of the evolution of the amplitudes $z_i(\tau)$ are also considered in eq. (2.11), for $i = 1, 2, 3$. The ansatz of the expansion is as follows

$$\mathbf{Q}(t,\tau) = \mathbf{Q}_0 + \varepsilon\mathbf{q}_{(\varepsilon)}(t,\tau) + \varepsilon^2\mathbf{q}_{(\varepsilon^2)}(t,\tau) + O(\varepsilon^3). \tag{2.7}$$

Herein, we evaluate the mode interaction between two steady symmetry breaking states with azimuthal wave number $m_1 = 1$ and $m_2 = 2$, that is,

$$\begin{aligned} \mathbf{q}_{(\varepsilon)}(t,\tau) \quad &= \left(z_1(\tau)\hat{\mathbf{q}}_{(z_1)}(r,z)e^{-\mathrm{i}m_1\theta} + \text{c.c.}\right) \\ &+\left(z_2(\tau)\hat{\mathbf{q}}_{(z_2)}(r,z)e^{-\mathrm{i}m_2\theta} + \text{c.c.}\right), \end{aligned} \tag{2.8}$$

where z_1 and z_2 are the complex amplitudes of the two symmetric modes $\hat{\mathbf{q}}_{(z_1)}$ and $\hat{\mathbf{q}}_{(z_1)}$. Note that the expansion of the LHS of eq. (2.3) up to third order is as follows

$$\varepsilon\mathbf{B}\frac{\partial\mathbf{q}_{(\varepsilon)}}{\partial t} + \varepsilon^2\mathbf{B}\frac{\partial\mathbf{q}_{(\varepsilon^2)}}{\partial t} + \varepsilon^3\left[\mathbf{B}\frac{\partial\mathbf{q}_{(\varepsilon^3)}}{\partial t}\right] + O(\varepsilon^4), \tag{2.9}$$

and the RHS respectively,

$$\mathbf{F}(\mathbf{q},\boldsymbol{\eta}) = \mathbf{F}_{(0)} + \varepsilon\mathbf{F}_{(\varepsilon)} + \varepsilon^2\mathbf{F}_{(\varepsilon^2)} + \varepsilon^3\mathbf{F}_{(\varepsilon^3)} + O(\varepsilon^4). \tag{2.10}$$

Then, the problem up to third order in z_1 and z_2 can be reduced to (Armbruster *et al.* 1988)

$$\begin{aligned} \dot{z}_1 \quad &= \lambda_1 z_1 + e_3\bar{z}_1 z_2 + z_1\left(c_{(1,1)}|z_1|^2 + c_{(1,2)}|z_2|^2\right), \\ \dot{z}_2 \quad &= \lambda_2 z_2 + e_4 z_1^2 + z_2\left(c_{(2,1)}|z_1|^2 + c_{(2,2)}|z_2|^2\right). \end{aligned} \tag{2.11}$$

where λ_1 and λ_2 are the unfolding parameters of the normal form. The procedure followed for the determination of the coefficients $c_{(i,j)}$ for $i, j = 1, 2$ and e_3 and e_4 is left to Appendix A. An exhaustive analysis of the nonlinear implications of this normal form on dynamics is left to section 5.

2.2.3. *Numerical methodology for stability tools*

Results presented herein follow the same numerical approach adopted by Fabre *et al.* (2019); Sierra *et al.* (2020*a*,*b*, 2021); Sierra-Ausin *et al.* (2022*a*,*b*), where a comparison with DNS can be found. The calculation of the steady-state, the eigenvalue problem and the normal form expansion are implemented in the open-source software `FreeFem++`. Parametric studies and generation of figures are collected by `StabFem` drivers, an open-source project available in https://gitlab.com/stabfem/StabFem. For steady-state, stability and normal form computations, we set the *stress-free* boundary condition at the outlet, which is the natural boundary condition in the variational formulation.

The resolution of the steady nonlinear Navier-Stokes equations is tackled by means of the Newton method. While, the generalised eigenvalue problem (eq. (2.5)) is solved following the Arnoldi method with spectral transformations. The normal form reduction procedure of section 2.2.2 only requires to solve a set of linear systems, which is also carried out within `StabFem`. On a standard laptop, every computation considered below can be attained within a few hours.

3. Characterisation of the axisymmetric steady-state

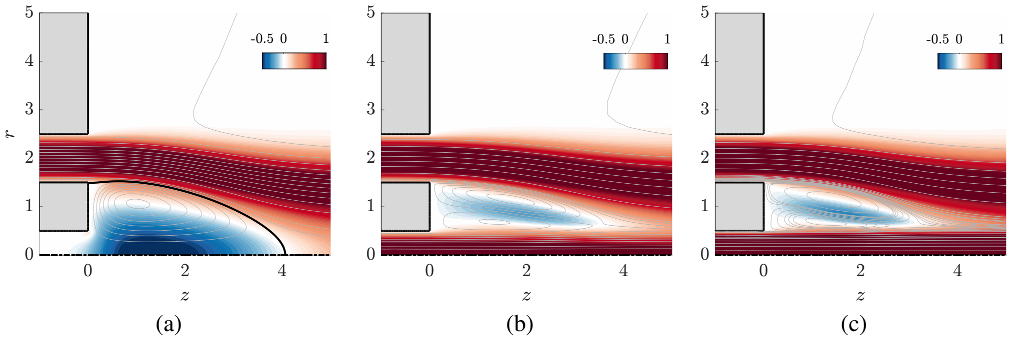

Figure 3: (Re = 400, L = 1) Meridional projections of the axisymmetric streamfunction isolines and the axial velocity contour in a range of $(z, r) \in [-1, 5] \times [0, 5]$. The large recirculation bubble is depicted with a thick black line. (a) $\delta_u = 0$. (b) $\delta_u = 1$. (c) $\delta_u = 2$.

The base flow is briefly described as a function of the inner-to-outer velocity ratio δ_u, the Reynolds number and the length L of the duct wall separating the two jet streams. We begin by characterising the development of the axisymmetric steady-state with varying δ_u at a constant Reynolds number fixed to Re = 400 and distance between the jets $L = 1$. The axial velocity component of the steady-state is illustrated in fig. 3 for three values of the velocity ratio. The most remarkable difference between them is the modification of the topology of the flow near the duct separating the two coaxial jet streams. The annular jet case ($\delta_u = 0$), represented in fig. 3 (a), displays a large recirculation bubble. On the other hand, for the velocity ratios $\delta_u = 1$ and $\delta_u = 2$ there is no longer a large recirculation bubble, but two closed regions of recirculating fluid near the duct separating the two coaxial jets. These last two cases are illustrated in fig. 3 (b-c).

Figure 4 displays the evolution of the recirculation length (L_r) associated with the large recirculating bubble, which characterises the configurations of coaxial jets with a low value of the velocity ratio δ_u. Figure 4(a) shows that the recirculation length is nearly constant for values of the velocity ratio δ_u smaller than the magnitude of the velocity vector in the recirculation region. The value of the plateau, for a constant duct wall distance L, increases with the Reynolds number. Reciprocally, at constant Reynolds number, the recirculation length increases with the duct wall length L separating the jet streams. For configurations of coaxial jets operated within this interval of the velocity ratio δ_u, we can say that the inner jet is trapped by the large recirculation region. Instead, when the velocity ratio δ_u is of similar magnitude to the axial velocity in the recirculating region, the inner jet is sufficiently energetic to break the recirculating region. For those values of the velocity ratio, the recirculation length is a rapidly decreasing function of δ_u. From fig. 4(a) we may conclude that larger distances between the jets respectively, a smaller value of the Reynolds

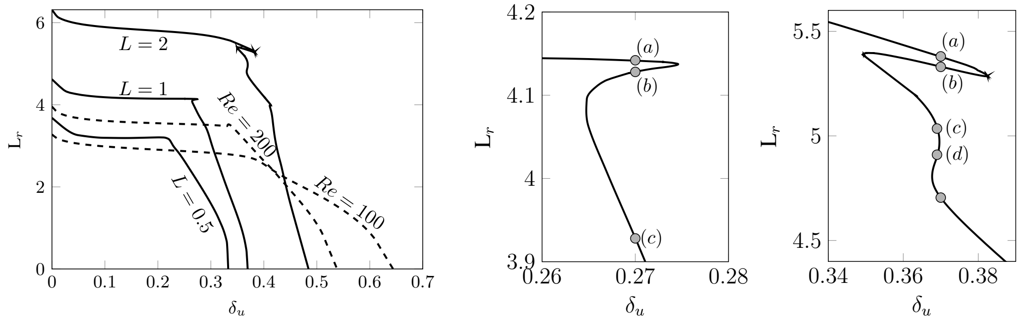

(a) (b) (c)

Figure 4: Evolution of the recirculation length (L_r) of the recirculating bubble with respect to the velocity ratio δ_u between the inner and outer jet. Solid lines are computed for a fixed Reynolds number $Re = 400$, while dashed lines are computed for a fixed distance $L = 1$. The figure (b) magnifies the region near the saddle-node bifurcation for $L = 1$, while figure (c) corresponds to an enlargement of the region near the saddle-node for $L = 2$.

number, lead to the existence of the recirculation region for larger velocity ratios. In addition, fig. 4 demonstrates the existence of multiple steady-states for the same velocity ratio. An enlargement of the region with multiple steady-states is displayed in Figure 4 (b) for the case of $L = 1$. It shows the existence of three steady-states in the interval of $0.265 \lesssim \delta_u \lesssim 0.275$, where the extreme points correspond to the location of the saddle-nodes. Figure 5 depicts the base flows associated with the circle markers in fig. 4 (b). Particularly, it demonstrates that the saddle-node bifurcations are, in some cases, associated with changes in the topology of the flow. From fig. 5 (a) to (b), one may appreciate the formation of a recirculating region along the duct wall separating the jet streams. While, from (b) to (c) we observe the formation of an additional region of recirculating flow near the upper corner of the duct wall. The large recirculation bubble is displaced downstream due to the formation of the two additional recirculation regions.

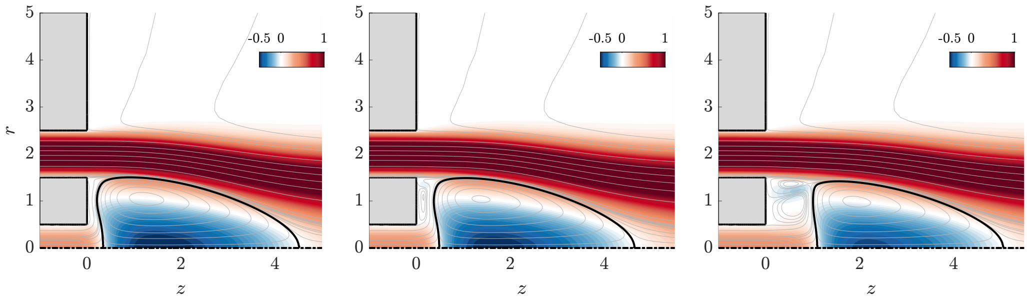

(a) (b) (c)

Figure 5: ($Re = 400$, $L = 1$) Meridional projections of the axisymmetric streamfunction isolines and the axial velocity contour in a range of $(z, r) \in [-1, 5] \times [0, 5]$. Each subfigure is associated to a marker of fig. 4 (b).

Figure 4 (c) corresponds to an enlargement of the region with multiple steady-states for a distance $L = 2$ between the jet streams. The base flows associated to the circle markers are illustrated in fig. 6. It demonstrates that changes in the flow topology do not always occur

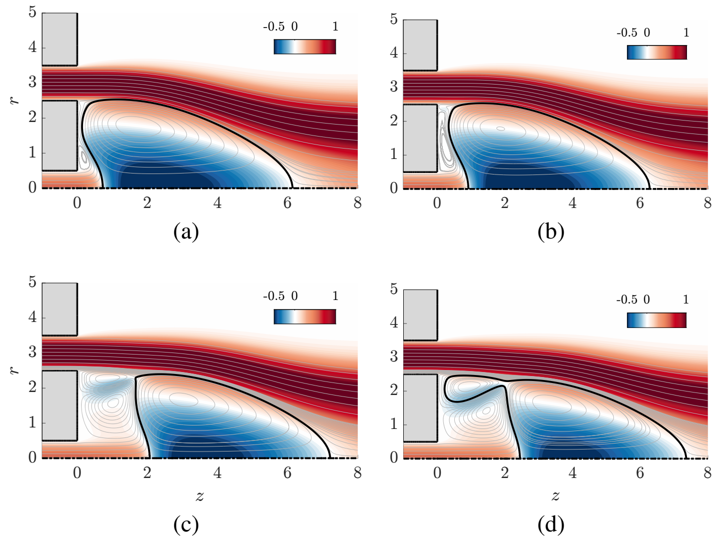

Figure 6: (Re = 400, L = 2) Meridional projections of the axisymmetric streamfunction isolines and the axial velocity contour in a range of $(z, r) \in [-1, 8] \times [0, 5]$. Each subfigure is associated to a marker of fig. 4 (c).

through saddle-node bifurcations. The base flow depicted in fig. 6 (a) already features a small region of a recirculating flow near the lower corner of the thick wall duct. Furthermore, from (a) to (b) we observe a stretching of the recirculation region attached to the duct wall, but without any change in the topology of the flow. On the contrary, the transitions from (b) to (c) and (c) to (d) are associated to changes in the topology of the flow. The passage from (b) to (c) is characterised by the formation of a vortex ring near the upper corner of the duct wall. Likewise, from (c) to (d) we appreciate a reconnection between the large recirculation bubble and the new vortex ring. Finally, the flow topology of the fifth steady-state, the circle marker without any text annotation, is identical to (d). In addition, it is worth noting that in the interval $0 < \delta_u < 2$ no further fold bifurcations are observed. Leading to the conclusion, that the saddle-node bifurcations are tightly connected to changes in the topology of the flow, leading to the disappearance of the large recirculation bubble and the formation of the two regions of recirculating fluid. Nonetheless, they are not neither the cause nor the effect of the modifications in the flow topology.

Lastly, the influence on the flow rate has been analysed, as the change of the distance between jets L, maintaining the same velocity profile on the outer jet, affects the value of the outer flow rate $\dot{V}_o \approx 5.4L$. On the other hand, the flow rate of the inner jet only depends on the inner-to-outer velocity ratio $\dot{V}_i \approx 3.7\delta_u$. As seen on figure 7, there are no significant changes on the recirculation bubble when the flow rate is changed. Figures 7 (b) and (c) show that similar cases with different flow rates but same ratio ($\frac{\dot{V}_o}{\dot{V}_i}$) between the inner and outer jet, present similar recirculation bubble.

Rapids articles must not exceed this page length

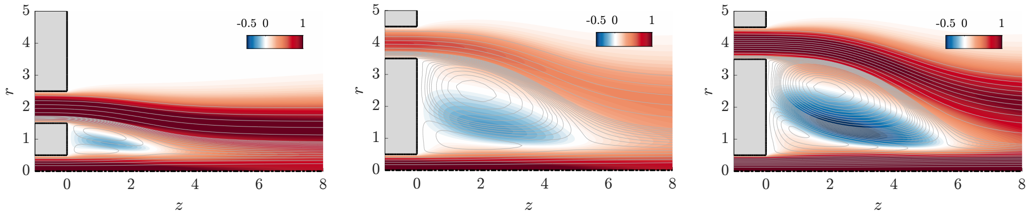

(a) (b) (c)

Figure 7: (Re = 200) Meridional projections of the axisymmetric streamfunction isolines and the axial velocity contour in a range of $(z, r) \in [-1, 5] \times [0, 8]$. (a) ($L = 1$, $\delta_u = 1$). (b) Duct wall length $L = 3$ and with the same flow rate of the outer jet ($\dot{V}_o$) of case (a). (c) ($L = 3$, $\delta_u = 2$) with the same ratio of the flow rate ($\dfrac{\dot{V}_o}{\dot{V}_i}$) between the inner and outer jet of cases (a) and (b)).

4. Linear stability analysis

4.1. *Spectrum*

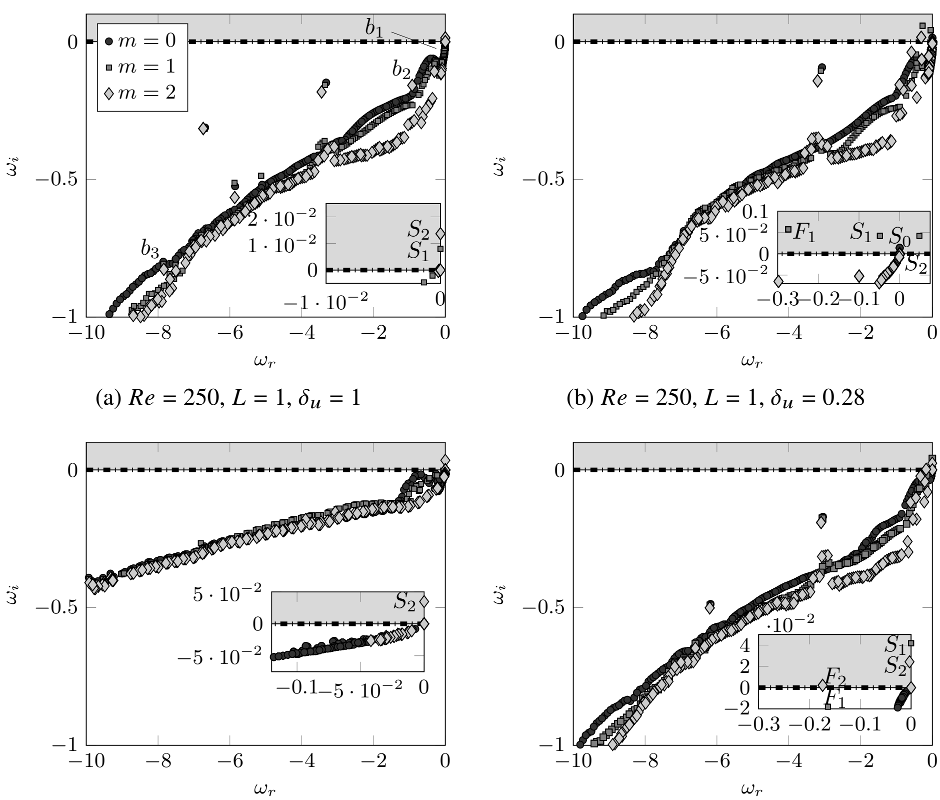

(a) Re = 250, L = 1, δ_u = 1
(b) Re = 250, L = 1, δ_u = 0.28
(c) Re = 800, L = 0.5, δ_u = 1
(d) Re = 250, L = 2, δ_u = 1

Figure 8: Spectrum computed at four different configurations of (Re, L, δ_u) for $m = 0, 1, 2$. The inset inside each subfigure magnifies the region near the origin. Stationary or low frequency modes are designated S, while oscillating/flapping modes are designated F, with the azimuthal wavenumber as the subscript.

Herein, we analyse the asymptotic linear stability of the steady-state in four distinct configurations. The first spectrum, depicted in fig. 8 (a), has been computed for a velocity ratio $\delta_u = 1$. Similarly, the second spectrum corresponds to a velocity ratio $\delta_u = 0.28$, which represents the middle branch after the saddle-node, that is, the equivalent of the marker (b) in fig. 4 (b) for $Re = 250$. These two configurations have been determined for a duct wall length $L = 1$. The remaining two spectrums have been computed for duct wall distances of $L = 0.5$ and $L = 2$, which are illustrated in fig. 8 (c) and fig. 8 (d), respectively. The computation of the spectrum reveals the existence of eigenmodes, with azimuthal wavenumbers $m = 0$, $m = 1$ and $m = 2$, that become unstable.

First, the four spectrums display three types of continuous branches, referred to as b_i

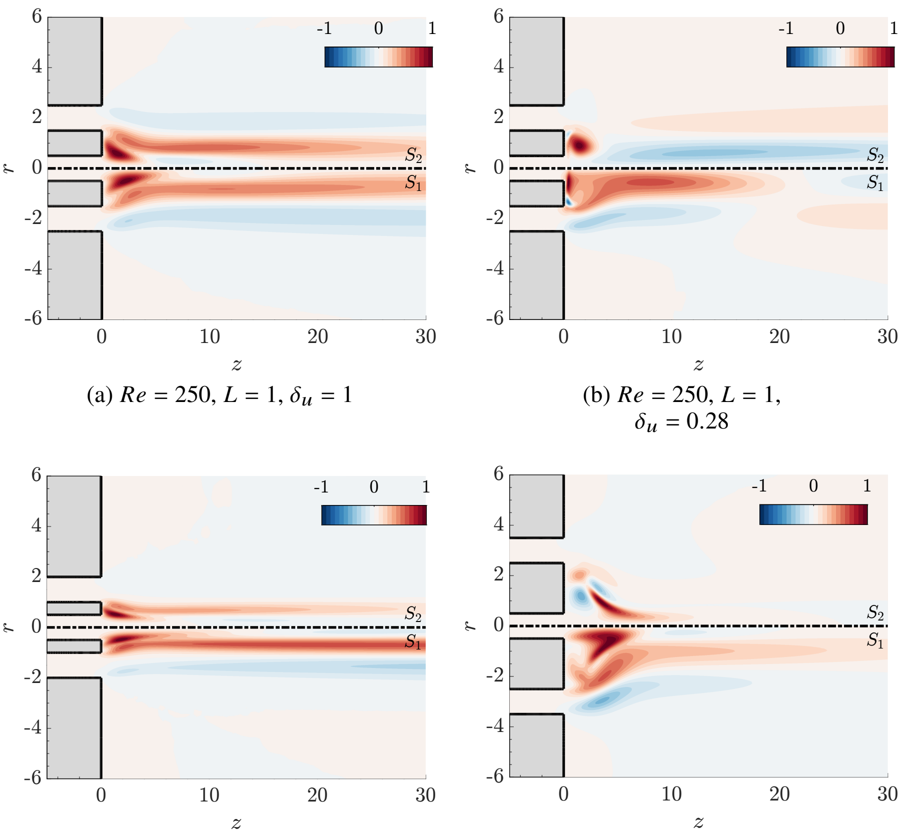

(a) $Re = 250$, $L = 1$, $\delta_u = 1$

(b) $Re = 250$, $L = 1$, $\delta_u = 0.28$

(c) $Re = 800$, $L = 0.5$, $\delta_u = 1$

(d) $Re = 250$, $L = 2$, $\delta_u = 1$

Figure 9: Axial velocity component of the non-oscillating global modes S_1 (bottom panel of the subfigure) and S_2 (top panel of the subfigure). The label of the subfigures coincide with the label of fig. 8.

($i = 1, 2, 3$), as it was the case in the configuration of coaxial jets described by Canton *et al.* (2017). The branch b_3 is composed of spurious modes. The branch b_2 is constituted of modes localised within the jet shear layers. While the branch b_1 is composed by nearly steady modes with support in the fluid region surrounding the jets.

Second, in the four configurations we find two *non-oscillating* unstable modes (or nearly neutral as it is the case in fig. 8 (c)) with azimuthal wavenumber $m = 1$ and $m = 2$, hereinafter referred to as modes S_1 and S_2, respectively. These two modes are depicted in fig. 9, which illustrates their axial velocity component for the four configurations. Their spatial distribution is mostly localised inside the recirculating region of the flow, but they are also supported along the shear layer of the jets. Evaluating both the direct and adjoint modes, we can identify the *core* of the global instability from the maximum values of the function $||\mathbf{S}_s(r,z)||_F$, which has been defined in eq. (2.6).

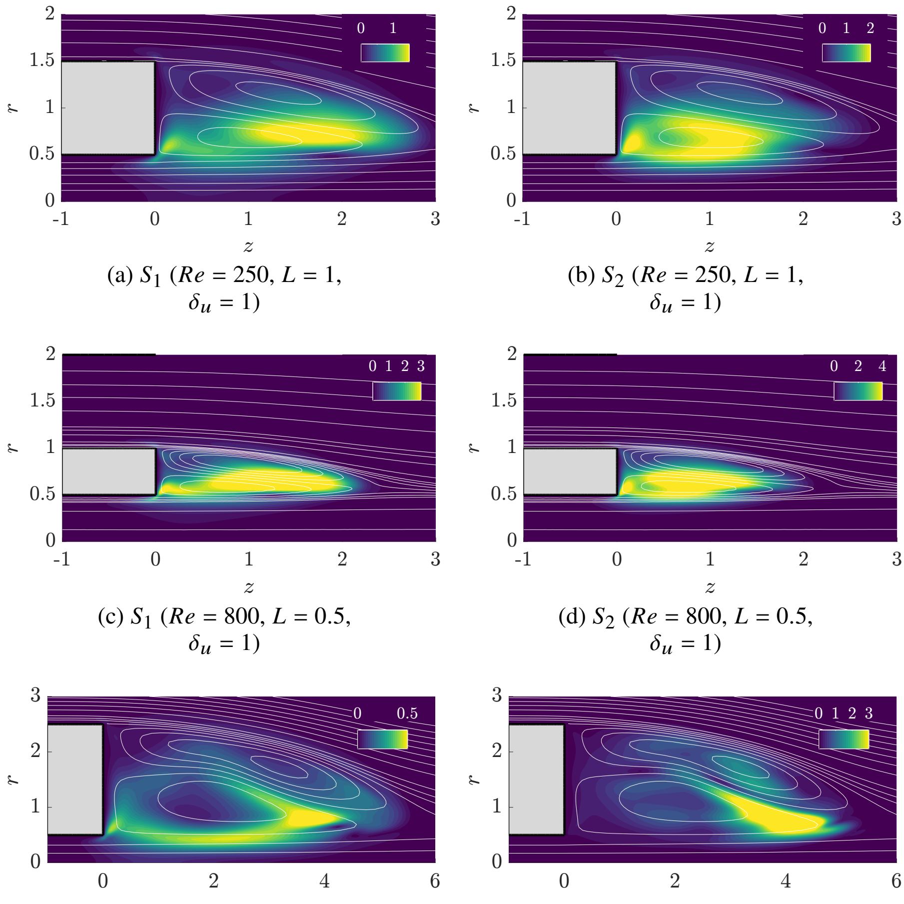

(a) S_1 ($Re = 250$, $L = 1$, $\delta_u = 1$)

(b) S_2 ($Re = 250$, $L = 1$, $\delta_u = 1$)

(c) S_1 ($Re = 800$, $L = 0.5$, $\delta_u = 1$)

(d) S_2 ($Re = 800$, $L = 0.5$, $\delta_u = 1$)

(e) S_1 ($Re = 250$, $L = 2$, $\delta_u = 1$)

(f) S_2 ($Re = 250$, $L = 2$, $\delta_u = 1$)

Figure 10: Structural sensitivity map $||\mathbf{S}_s(r,z)||_F$. White lines are employed to represent the steady-state streamlines.

Figure 10 illustrates the sensitivity maps for the modes displayed in fig. 9 (a,c,d). The sensitivity maps $||\mathbf{S}_s(r,z)||_F$ are compact supported within the region of recirculating fluid, featuring negligible values elsewhere. The maximum values of the sensitivity maps, displayed in fig. 10 (a,c,e) for the mode S_1, are found within the inner vortex ring, in particular near the downstream part of the inner vortical region, and on the interface between the two vortical rings. By increasing the wall length separating the jet streams, the wavemaker moves downstream towards the right end of the inner vortical region. A similar observation is drawn from fig. 10 (b,d,f), where the core of the instability is also found within the inner vortex ring.

Similar observations were drawn in the case of the wake behind rotating spheres (Sierra-Ausín *et al.* 2022), where the core of the instability was also found near the downstream part of the recirculating flow region. Therein, it was concluded that the instability is supported by the recirculating flow region.

Figure 8 (d) illustrates the existence of two *oscillating/flapping* modes with azimuthal

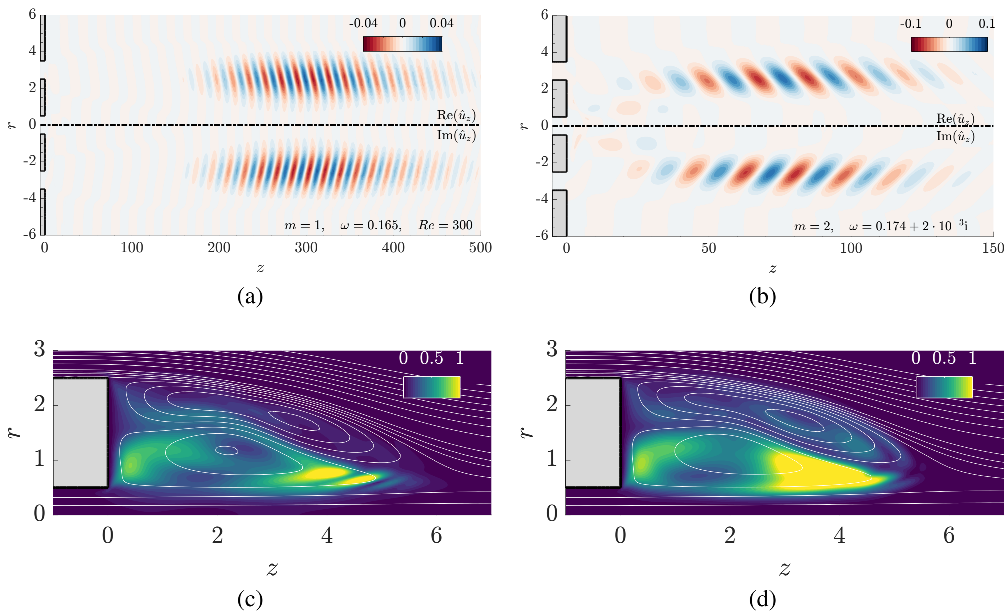

Figure 11: Axial velocity component of the oscillating global modes F_1 (a) and F_2 (b). Structural sensitivity map $||\mathbf{S}_s(r,z)||_F$ of mode F_1 (c) and F_2 (d). White lines are employed to represent the steady-state streamlines.

wavenumber $m = 1$ and $m = 2$, hereinafter referred to as F_1 and F_2, respectively. The axial velocity component of these two modes is displayed in fig. 11, together with their associated structural sensitivity map. The unsteady modes F_1 and F_2 possess a much larger spatial support than S_1 and S_2. They are formed by an array of counter-rotating vortex spirals sustained along the shear layer of the base flow. For the mode F_2 the amplitude of these structures grows downstream of the nozzle, in the axial direction, with a maximum around $z \approx 70$, after which they slowly decay. The mode F_1 grows further downstream, with a maximum around $z \approx 300$. The spatial structure of these eigenmodes resembles the axisymmetric mode of Figure 9 in Canton *et al.* (2017) or the optimal response modes determined by Montagnani & Auteri (2019). As it was the case for the non-oscillating modes, the core of the instability is found near the downstream part of the inner vortex ring. Tentatively, one may conclude that vortical perturbations are produced within the recirculating flow region and convected downstream while experiencing a considerable spatial amplification, which in turn justifies the resemblance with the optimal response modes determined by Montagnani & Auteri (2019).

There is an unstable $m = 0$ mode, hereinafter referred to as S_0, in the spectrum displayed in Figure 8 (b). Such a mode, which is illustrated fig. 12 (a), is the result of a saddle-node bifurcation leading to the existence of multiple steady-states, a feature that has been discussed in section 3. It is a mode that promotes the formation of a recirculating flow region attached to the duct wall. In section 3 we have remarked that the S_0 modes can be related to changes

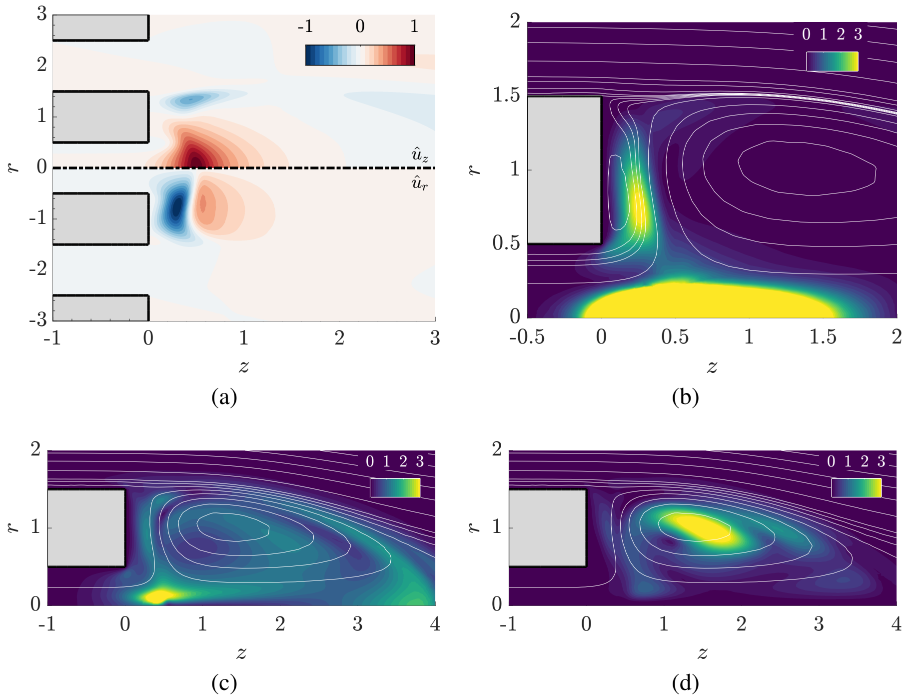

Figure 12: (a) Global mode S_0 for the configuration (Re = 250, L = 1, δ_u = 0.28). The top panel of (a) represents the axial velocity, while the bottom panel depicts the radial velocity component. Structural sensitivity map $||\mathbf{S}_s(r,z)||_F$ of the mode S_0 (b), S_1 (c) and S_2 (d). White lines are employed to represent the steady-state streamlines.

in the topology of the flow, and to a downstream shift of the recirculation bubble. Thus, it is not surprising that the core of the instability, shown in fig. 12 (b), is found on the interface between the recirculating region attached to the wall and the large recirculation bubble, and mostly in a region close to the axis found near the leftmost end of the recirculation bubble. The changes in the base flow due to the S_0 mode have an impact on the instability core of the S_1 and S_2 modes, which are depicted in fig. 12 (c) and (d), respectively. The maximum values of the structural sensitivity are found on the leftmost end of the recirculation bubble near the axis of revolution, while it is found in the centre of the recirculation bubble for the mode S_2.

4.2. *Annular jet configuration* $\delta_u = 0$

Herein, we investigate the effect of the duct wall length ($0.5 < L < 4$) on the linear stability of the annular jet ($\delta_u = 0$).

The linear stability findings are summarised in fig. 13, which displays the evolution of the critical Reynolds number with respect to the duct wall distance (L) for the four most unstable modes: two non-oscillating S_1 and S_2, and two oscillating F_1 and F_2. A cross-section view at $z = 1$ is displayed in fig. 14. Please note that for the chosen set of parameters the axisymmetric unsteady mode F_0, is always found at larger Reynolds numbers than the aforementioned modes, that is why in the following, we only include the results for the S_1, S_2, F_1 and F_2 modes. This is one of the major differences with the case studied by Canton *et al.* (2017). For small values of the duct wall length ($L \approx 0.1$) separating the jet streams, the dominant instability is a vortex-shedding mode, which in our nomenclature is referred

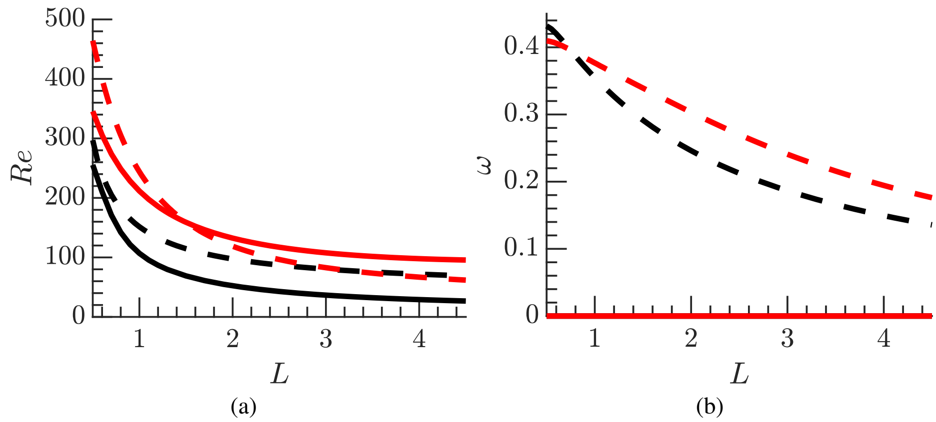

Figure 13: Linear stability boundaries for the annular jet ($\delta_u = 0$). (b) Frequency evolution of the unsteady modes. Legend: S_1 mode is displayed with a solid black line, S_2 with a solid red line and F_1 and F_2 modes are depicted with dashed black and red lines, respectively.

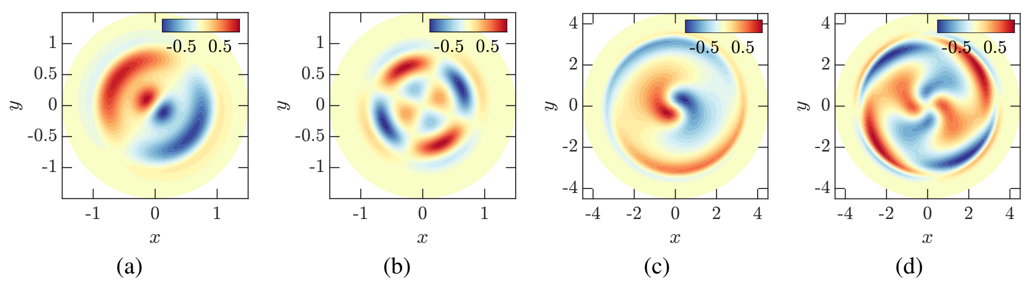

Figure 14: Cross-section view at $z = 1$ of the four unstable modes at criticality for the annular jet case ($\delta_u = 0$). The streamwise component of the vorticity vector ϖ_z is visualised by colours. (a) Mode S_1 for $L = 0.5$, (b) Mode S_2 for $L = 0.5$, (c) Mode F_1 for $L = 3$ and (d) Mode F_2 for $L = 3$.

to as F_0. On the contrary, for duct wall lengths in the interval $0.5 < L < 4$, the primary instability of the annular jet is a steady symmetry-breaking bifurcation that leads to a jet flow with a single symmetry plane, displayed in fig. 14 (a). In contrast, bifurcations that lead to the mode S_2 possess two orthogonal symmetry planes, see fig. 14 (b). In section 4.1 it has been established that non-oscillating modes S_1 and S_2 for $\delta_u = 1$ display most of its compact support within the region of recirculating fluid. Likewise, in the annular jet configuration, fig. 15 demonstrates that the spatial distribution of these two stationary modes S_1 and S_2 is found inside the recirculation bubble. For jet distances $L < 2$, the second mode that bifurcates is F_1 mode, depicted in fig. 16 (a). This situation corresponds to a bifurcation scenario similar to other axisymmetric flow configurations, such as the flow past a sphere or a disk (Auguste *et al.* 2010; Meliga *et al.* 2009). For larger distances between jets, the scenario changes. The second bifurcation from the axisymmetric steady-state is the F_2, displayed in fig. 16 (b). Other configurations where the primary or secondary instability involves modes with azimuthal component $m = 2$ are swirling jets (Meliga *et al.* 2012) and the wake flow past a rotating sphere (Sierra-Ausín *et al.* 2022). The unsteady modes F_1 and F_2 display a similar structure to the unsteady modes discussed in section 4.1. They are formed by an

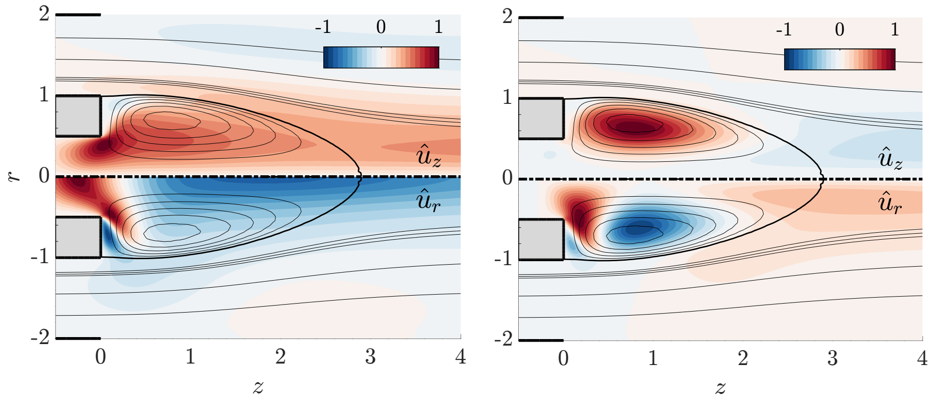

(a) (b)

Figure 15: Global modes S_1 (a) and S_2 (b) at criticality for $L = 0.5$ and $\delta_u = 0$. The top panel of (a) represents the axial velocity, while the bottom panel depicts the radial velocity component. Black lines represent the streamlines of the base flow.

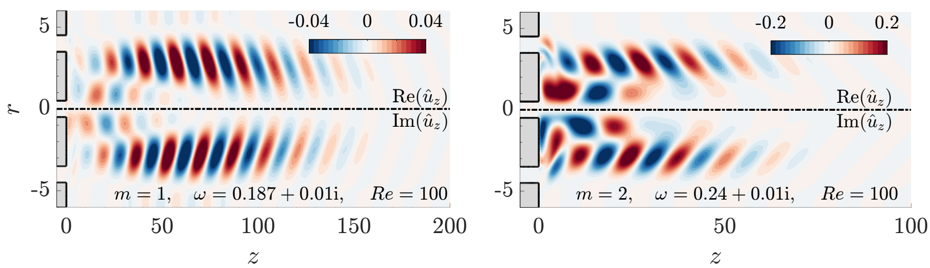

(a) (b)

Figure 16: Axial velocity component of the neutral modes for $L = 3$ and $\delta_u = 0$ (a) F_1, (b) F_2 .

array of counter-rotating vortex spirals developing in the wake of the separating duct wall and convected downstream, while experiencing an important spatial amplification until they eventually decay after reaching a maximum amplitude.

4.3. *Fixed distance between jets and variable velocity ratio δ_u*

In the following, we focus on the influence of the velocity ratio δ_u between jets for fixed jet distances L. Figure 17 displays the neutral curve of stability for jet distances (a) $L = 0.5$ and (b) $L = 1$. One may observe that the primary bifurcation is not always associated to the mode S_1 as it is the case for $\delta_u = 0$. For sufficiently large velocity ratios, the primary instability leads to a non-axisymmetric steady-state with a double helix, corresponding to the unstable mode S_2. As can be appreciated in fig. 9 (b), for small values of δ_u, the mode S_1 expands downstream over a relatively large area, having a higher activity than mode S_2, which is confined to the recirculation region. As the ratio between velocities is increased, as observed in fig. 9 (a), mode S_2 enlarges and resembles to mode S_1, controlling the instability mechanism for large values of δ_u. Another interesting feature, which could motivate a control strategy, is the occurrence of vertical asymptotes. This sudden change in the critical Reynolds number is due to the retraction, disappearance of the recirculation bubble and the formation of a new recirculating flow region, aspects that have been covered in section 3. For $L = 0.5$,

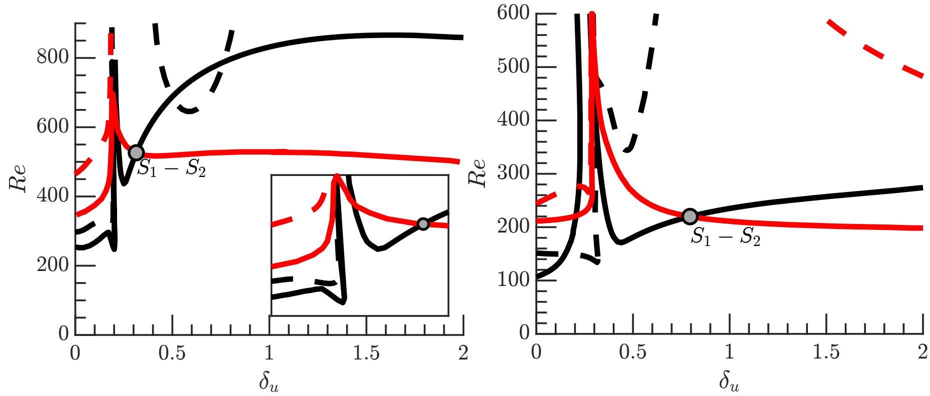

(a) (b)

Figure 17: Linear stability boundaries for the concentric jets (a) $L = 0.5$ and (b) $L = 1$. Same legend as fig. 13.

this sudden change occurs for $\delta_u \approx 0.25$, and for higher values of δ_u the critical Reynolds number is around twice larger than the one of the annular jet ($\delta_u = 0$). The case of jet distance $L = 1$ was discussed in section 3. The sudden change in the stability of the branch S_1 occurs between $\delta_u \in [0.25, 0.5]$. Within this narrow interval, the primary branch of instability is the F_1. At around $\delta_u = 0.4$, the primary bifurcation is again the branch S_1, which becomes secondary at around $\delta_u \approx 0.8$ in favour of the branch S_2. In fig. 17 we have highlighted the codimension two point interaction between the $S_1 - S_2$ modes, which will be analysed in detail in section 5. Around this point, we can observe the largest ratio $(\frac{Re_c|_{\delta_u \neq 0}}{Re_c|_{\delta_u = 0}})$ between the value of the critical Reynolds number of the primary instability for a concentric jet configuration ($\delta_u \neq 0$) and the annular jet problem ($\delta_u = 0$).

4.4. *Fixed velocity ratio δ_u and variable distance between jets*

Figure 18 compares the results obtained for a constant velocity ratio when varying the distance between jets. As observed before, the increase of the distance between the jets has a de-stabilising effect. The largest critical Reynolds number is found at $\delta_u = 0$, and the critical Reynolds number decreases with the duct wall length L between the jet streams. The points of codimension two are highlighted in fig. 18. We can appreciate that the interaction between the branch S_1 and S_2 happens for every velocity ratio δ_u explored, and it is the mode interaction associated to the smallest distance between jets. Additionally, for a velocity ratio $\delta_u = 0.5$ there exist two points where the branches of the linear modes S_1 and F_1 intersect. Another feature of the neutral curves is the existence of turning points, which are associated to the existence of saddle node bifurcations of the axisymmetric steady-state, addressed in section 3. The saddle-node bifurcations of the steady-state induce the existence of regions in the neutral curves with a *tongue* shape. These saddle node bifurcations are also responsible for the formation of the vertical asymptotes observed in fig. 17. Finally, it is of interest the transition of the modes S_1 and S_2, which induce the symmetry breaking of the axisymmetric steady state to slow low frequency spiralling structures. These modes have been identified for $\delta_u = 0.5$ for $m = 1$, $\delta_u = 1$ for $m = 2$, and $\delta_u = 2$ for both $m = 1$ and $m = 2$. As it will be clarified in section 5, these oscillations are issued from the non-linear interaction of modes, emerging simultaneously for a specific Reynolds number, and changing their position as the most unstable global mode of the flow.

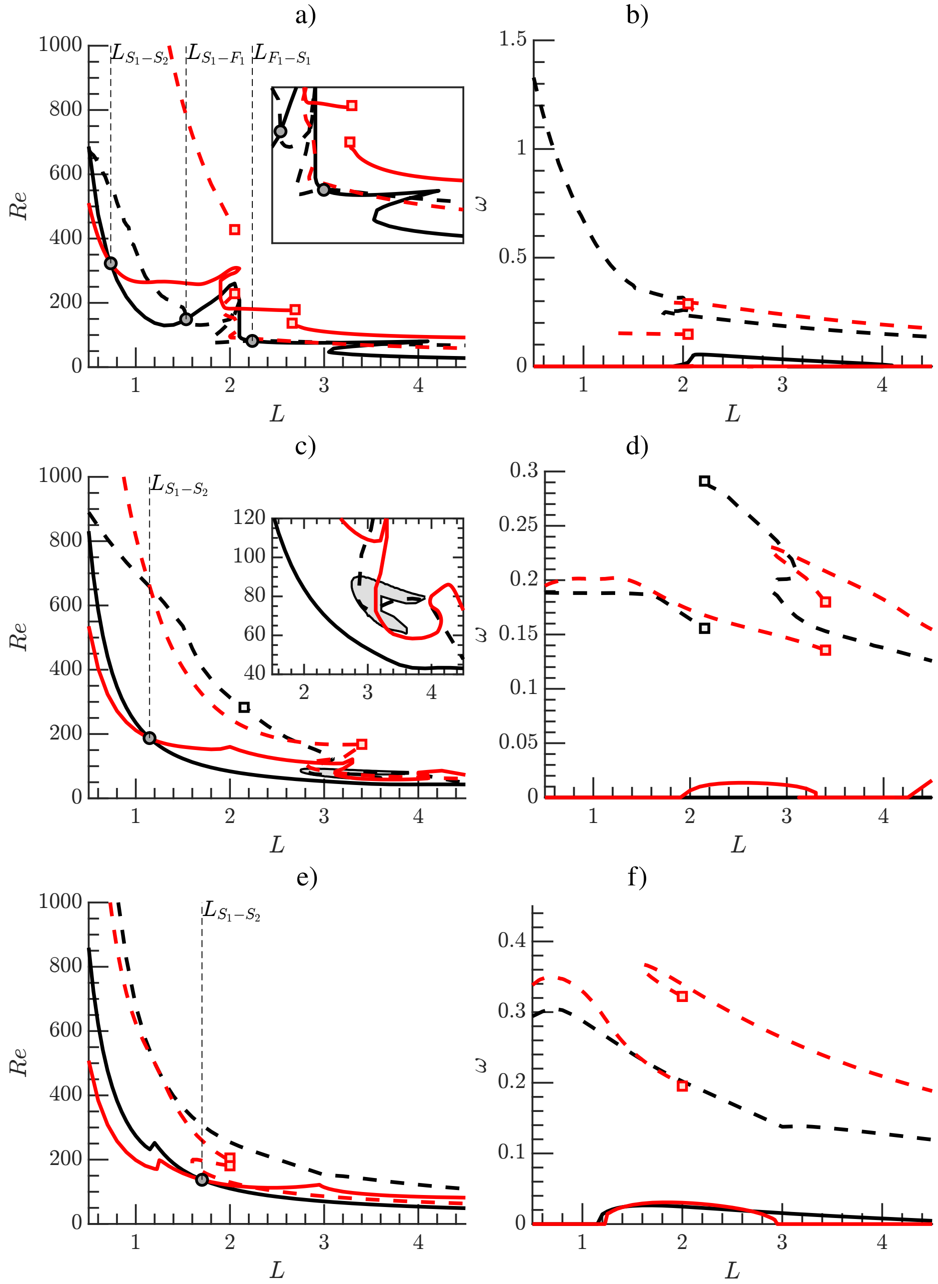

Figure 18: Neutral lines of the four modes found studying the configuration of two concentric jets fixing the velocity ratio. (a-b) δ_u = 0.5, (c-d) δ_u = 1, (e-f) δ_u = 2. Black lines: modes with m = 1, red lines: modes with m = 2. Straight lines: steady modes, dashed lines: unsteady modes. The discontinuity points, i.e., the points where the second most unstable mode (of a given type) becomes the most unstable are highlighted with square markers.

5. Mode interaction between two steady states. Resonance 1 : 2

5.1. *Normal form, basic solutions and their properties*

The linear diagrams of section 4 have shown the existence of the mode interaction between the modes S_1 and S_2. It corresponds roughly to the mode interaction that occurs at the largest critical Reynolds number for any value of L herein explored. In this section, we analyse the dynamics near the $S_1 : S_2$ organising centre. We perform a normal form reduction, which allows us to predict non-axisymmetric steady, periodic, quasiperiodic and heteroclinic cycles between non-axisymmetric states.

The mode interaction that is herein analysed corresponds to a steady-steady bifurcation with $O(2)$ symmetry and with strong resonance $1 : 2$. Such a bifurcation scenario has been extensively studied in the past by (Dangelmayr 1986; Jones & Proctor 1987; Porter & Knobloch 2001; Armbruster *et al.* 1988) and the reflection symmetry breaking case (SO(2)) by Porter & Knobloch (2005). In order to unravel the existence and the stability of the nonlinear states near the codimension two point, let us write the flow field as

$$\mathbf{q} = \mathbf{Q}_0 + \mathrm{Re}\left[r_1(\tau)e^{i\phi_1(\tau)}e^{-i\theta}\hat{\mathbf{q}}_{s,1}\right] + \mathrm{Re}\left[r_2(\tau)e^{i\phi_2(\tau)}e^{-2i\theta}\hat{\mathbf{q}}_{s,2}\right] \tag{5.1}$$

in polar coordinates for the complex amplitudes $z_1 = r_1 e^{i\phi_1}$ and $z_2 = r_2 e^{i\phi_2}$ where r_j and ϕ_j for $j = 1, 2$ are the amplitude and phase of the symmetry-breaking modes $m = 1$ and $m = 2$, respectively. The complex-amplitude normal form eq. (2.11) is expressed in this reduced polar notation as follows,

$$\dot{r}_1 = e_3 r_1 r_2 \cos(\chi) + r_1\left(\lambda_{(s,1)} + c_{(1,1)} r_1^2 + c_{(1,2)} r_2^2\right), \tag{5.2a}$$

$$\dot{r}_2 = e_4 r_1^2 \cos(\chi) + r_2\left(\lambda_{(s,2)} + c_{(2,1)} r_1^2 + c_{(2,2)} r_2^2\right), \tag{5.2b}$$

$$\dot{\chi} = -\left(2e_3 r_2 + e_4 \frac{r_1^2}{r_2}\right)\sin(\chi), \tag{5.2c}$$

where the phase $\chi = \phi_2 - 2\phi_1$ is coupled with the amplitudes r_1 and r_2 because of the existence of the $1 : 2$ resonance. The individual phases evolve as

$$\begin{aligned} \dot{\phi}_1 &= e_3 r_2 \sin(\chi), \\ \dot{\phi}_2 &= -e_4 \frac{r_1^2}{r_2} \sin(\chi). \end{aligned} \tag{5.3}$$

Before proceeding to the analysis of the basic solutions of eq. (5.2), we can simplify these equations by the rescaling

$$\left(\frac{r_1}{|e_3 e_4|^{1/2}}, \frac{r_2}{e_3}\right) \to (r_1, r_2),$$

which yields the following equivalent system

$$\dot{r}_1 = r_1 r_2 \cos(\chi) + r_1\left(\lambda_{(s,1)} + c_{11} r_1^2 + c_{12} r_2^2\right), \tag{5.4a}$$

$$\dot{r}_2 = s r_1^2 \cos(\chi) + r_2\left(\lambda_{(s,2)} + c_{21} r_1^2 + c_{22} r_2^2\right), \tag{5.4b}$$

$$\dot{\chi} = -\frac{1}{r_2}\left(2r_2^2 + s r_1^2\right)\sin(\chi), \tag{5.4c}$$

where the coefficients

$$s = \mathrm{sign}(e_3 e_4), \quad c_{11} = \frac{c_{(1,1)}}{|e_3 e_4|}, \quad c_{12} = \frac{c_{(1,2)}}{e_3^2}, \quad c_{21} = \frac{c_{(2,1)}}{|e_3 e_4|}, \quad c_{22} = \frac{c_{(2,2)}}{e_3^2}.$$

Name	Definition	Bifurcations	Comments
O	$r_{1,O} = r_{2,O} = 0$	–	Steady axisymmetric state
P	$r^2_{2,P} = \frac{-\lambda_{(s,2)}}{c_{22}},\ r_{1,P} = 0$	$\lambda_{(s,2)} = 0$	Bifurcation from O
MM	$r_{1,MM} = -\frac{\lambda_{(s,1)} \pm r_{2,MM} + c_{12} r^2_{2,MM}}{c_{11}}$ $\mathrm{P_{MM}}(r_{2,MM}\cos(\chi_{MM})) = 0$ $\cos(\chi_{MM}) = \pm 1$	$\lambda_{(s,1)} = 0$ $\sigma_\pm = 0$	Bifurcation from O Bifurcation from P
TW	$\cos(\chi_{TW}) = \frac{(2c_{11}+c_{12})\lambda_{(s,2)} - (2c_{21}+c_{22})\lambda_{(s,1)}}{\Sigma_{TW}(2\lambda_{(s,1)}+\lambda_{(s,2)})}$ $r^2_{2,TW} = \frac{-(2\lambda_{(s,1)}+\lambda_{(s,2)})}{\Sigma_{TW}}$ $r^2_{1,TW} = 2r^2_{2,TW}$	$\cos(\chi_{TW}) = \pm 1$	Bifurcation from MM

Table 1: Definition of the fixed points of the reduced polar normal form eq. (5.4). $\sigma_\pm$ is defined in eq. (5.6), the polynomial P_{MM} is defined in eq. (5.7) and $\Sigma_{TW} \equiv 4c_{11} + 2(c_{12} + c_{21}) + c_{22}$.

Finally, we consider a third normal form equivalent to the previous ones but which removes the singularity of eqs. (5.2) and (5.4) when $r_2 = 0$. Standing waves ($\sin\chi = 0$) naturally encounter this type of artificial singularity, which manifests as in eq. (5.4) as an instantaneous jump from one standing subspace to the other by a π-translation. This is the case of the heteroclinic cycles, previously studied by Armbruster *et al.* (1988); Porter & Knobloch (2001). The third normal form, which we shall refer to as reduced Cartesian normal form, takes advantage of the simple transformation $x = r_2\cos(\chi)$, $y = r_2\sin(\chi)$ (Porter & Knobloch 2005):

$$\dot r_1 = r_1\Big(\lambda_{(s,1)} + c_{11}r_1^2 + c_{12}(x^2+y^2) + x\Big), \tag{5.5a}$$

$$\dot x = sr_1^2 + 2y^2 + x\Big(\lambda_{(s,2)} + c_{21}r_1^2 + c_{22}(x^2+y^2)\Big), \tag{5.5b}$$

$$\dot y = -2xy + y\Big(\lambda_{(s,2)} + c_{21}r_1^2 + c_{22}(x^2+y^2)\Big), \tag{5.5c}$$

In this final representation standing wave solutions are contained within the invariant plane $y = 0$, and due to the invariance of eq. (5.5) under the reflection $y \mapsto -y$, one can restrict attention, without loss of generality, to solutions with $y \geqslant 0$, cf Porter & Knobloch (2001).

The system eq. (5.4) possess four types of fixed points, which are listed in table 1.

First, the axisymmetric steady state (O) is represented by $(r_1, r_2) = (0, 0)$, so it is the trivial steady-state of the normal form. The second steady-state is what it is denoted as pure mode (P). In the original coordinates, it corresponds to the symmetry breaking structure associated to the mode S_2. This state bifurcates from the axisymmetric steady state (O) when $\lambda_{(s,2)} = 0$. The third fixed point is the mixed mode state (MM), which is listed in table 1. It corresponds to the reflection symmetry preserving state associated to the mode S_1. It may bifurcate directly from the trivial steady state O, when $\lambda_{(s,1)} = 0$ or from P whenever $\sigma_+ = 0$ or $\sigma_- = 0$, where $\sigma_\pm$ is defined as

$$\sigma_\pm \equiv \lambda_{(s,1)} - \frac{-\lambda_{(s,2)}c_{12}}{c_{22}} \pm \sqrt{\frac{-\lambda_{(s,2)}}{c_{22}}}. \tag{5.6}$$

Name	Bifurcation condition	Comments
SW	$sr_1^2 - 2c_{11}r_1^2 r_{2,MM}\cos(\chi_{MM}) - 2c_{22}r_{2,MM}^3\cos(\chi_{MM})^3 = 0$	Bif. from MM
MTW	$D_{TW} - T_{TW}I_{TW} = 0$, $I_{TW} > 0$	Bif. from TW

Table 2: Definition of the limit cycles of the reduced polar normal form eq. (5.4).

The representation in the reduced polar form is

$$r_{1,MM} = -\frac{\lambda_{(s,1)} \pm r_{2,MM} + c_{12}r_{2,MM}^2}{c_{11}}, \qquad \cos(\chi_{MM}) = \pm 1,$$

and the condition $\mathrm{P}_{\mathrm{MM}}(r_{2,MM}\cos(\chi_{MM})) = 0$, where P_{MM} is defined as

$$\mathrm{P}_{\mathrm{MM}}(x) \equiv s\mu_1 + (s + c_{21}\lambda_{(s,1)} - c_{(1,1)}\lambda_{(s,2)})x + (c_{21} + sc_{12})x^2 + (c_{12}c_{21} - c_{11}c_{22})x^3. \quad (5.7)$$

Finally, the fourth fixed point of the system are travelling waves (TW). It is surprising that the interaction between two steady-states causes a time-periodic solution. The travelling wave emerges from MM in parity-breaking pitchfork bifurcation that breaks the reflection symmetry when $\cos(\chi_{TW}) = \pm 1$. The TW drifts at a steady rotation rate ω_{TW} along the group orbit, i.e., the phases $\dot{\phi}_1 = r_{2,TW}\sin(\chi_{TW})$ and $\dot{\phi}_2 = -s\frac{r_{1,TW}^2}{r_{2,TW}}\sin(\chi_{TW})$ are non-null.

Mixed modes and travelling waves may further bifurcate into standing waves (SW) and modulated travelling waves (MTW), respectively. These are generic features of the $1:2$ resonance for small values of $\lambda_{(s,1)}$ and $\lambda_{(s,2)}$, when $s = -1$. In the original coordinates, SW are periodic solutions, whereas MTW are quasiperiodic. Standing waves emerge via a Hopf bifurcation from MM when the conditions $\mathrm{P}_{\mathrm{SW}}\Big(r_{2,MM}\cos(\chi_{MM})\Big) > 0$ for

$$\mathrm{P}_{\mathrm{SW}}(x) \equiv (2c_{22}x^3 - sr_1^2)c_{11} - (2c_{12}x + 1)(c_{21}x + s)x,$$

and the one listed in table 2 are satisfied. MTW are created when a torus bifurcation happens on the travelling wave branch when the conditions listed in table 2 are satisfied.

Another remarkable feature of eq. (5.2) is the existence of robust heteroclinic cycles that are asymptotically stable. When $s = -1$, there are open sets of parameters where the reduced polar normal form exhibits structurally stable connections between $\pi-$translations on the circle of pure modes, cf Armbruster *et al.* (1988). These structures are robust and have been observed in a large variety of systems, (Nore *et al.* 2003, 2005; Mercader *et al.* 2002; Palacios *et al.* 1997; Mariano & Stazi 2005). In addition to these robust heteroclinic cycles connecting pure modes, there exist more complex limit cycles connecting O, P, MM and SW, cf Porter & Knobloch (2001). These cycles are located for larger values of $\lambda_{(s,1)}$ and $\lambda_{(s,2)}$, with possibly chaotic dynamics (Shilnikov type). In this study, we have not identified any of these. Finally, a summary of the basic solutions and the bifurcation path is sketched in fig. 19.

5.2. *Results of the steady-steady* $1:2$ *mode interaction*

Section 4.4 reported the location of mode interaction points for discrete values of the velocity ratio δ_u. The location of the mode interaction between S_1 and S_2 is depicted in fig. 20. It shows that the mode switching between the modes S_1 and S_2 is indeed stationary only for $\delta_u < 1.5$ and $L < 1.3$. For larger values of the velocity ratio and the jet distance, the interaction is not purely stationary; at least one of the linear modes oscillates with a slow frequency. It implies

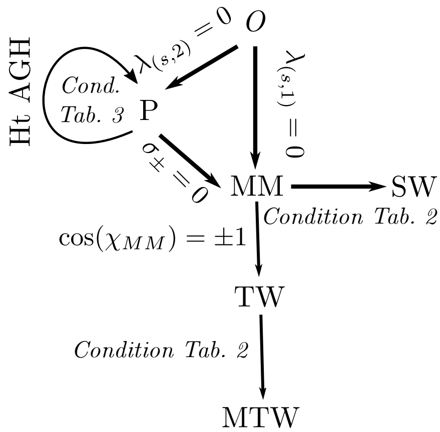

Figure 19: Schematic representation of the basic solutions of eq. (5.2) and their bifurcation path.

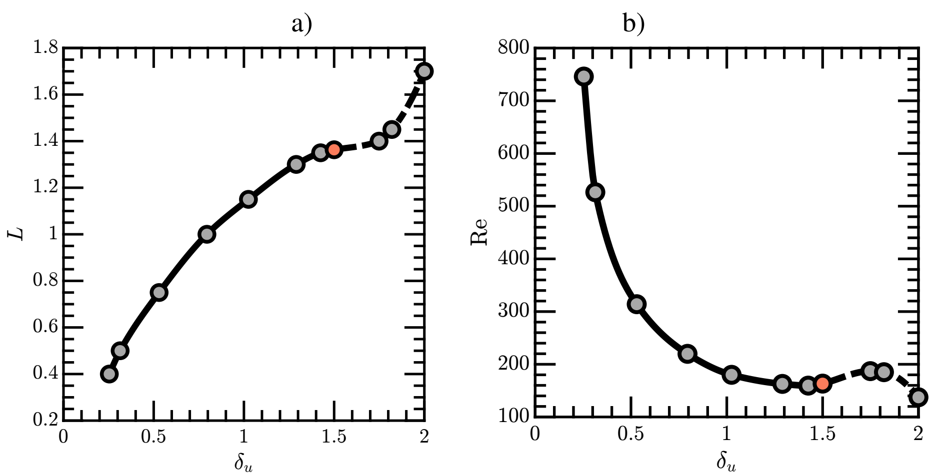

Figure 20: Evolution of the codimension two interaction $S_1 - S_2$ in the space of parameters $(\mathrm{Re}, L, \delta_u)$. Grey points denote the points that were computed and the red point denotes the transition from steady to unsteady with low frequency as reported in section 4.4.

that the mode selection for large velocity ratios near the codimension two points is similar to the one reported by Meliga *et al.* (2012) for swirling jets. However, even when the two primary bifurcations are non-oscillating (S_1 and S_2), the $1:2$ resonance of the azimuthal wavenumbers induces a slow frequency, what we denote as travelling wave solutions (TW).

We consider the bifurcation sequence for $\delta_u = 1.0$ and $L = 1.15$, which is qualitatively similar to transitions in the range $0.5 < \delta_u < 1.5$, near the codimension two points, which are depicted in fig. 20. At the codimension two points for $\delta_u < 0.5$, at least one of the two bifurcations is sub-critical and a normal form reduction up to fifth order is necessary. Subcritical transition was also noticed for a distance between jets $L = 0.1$ by Canton *et al.* (2017), who reported high levels of the linear gain associated to transient growth mechanisms. This last case is out of the scope of the present manuscript. Figure 21 displays the phase portrait of the stable attractors near the $S_1 : S_2$ interaction. For values of $\delta_u > 1.0$, the axisymmetric steady-state loses its axisymmetry leading to a new steady-state with symmetry

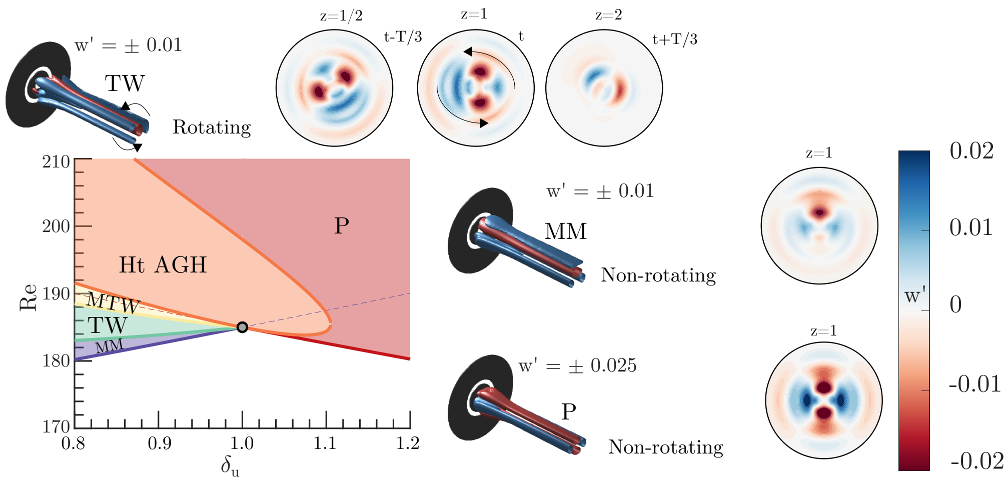

Figure 21: Parametric portrait at the codimension two point $S_1 : S_2$ for parameter values $(L, \delta_u) = (1.15, 1.0)$. The colour-shaded areas corresponds to the regions in the parameter space where a given solution is attracting, e.g., the green-shaded area is the region where TW is the attracting solution. Solid lines indicate codimension-one bifurcations, dashed-lines indicate when $\lambda_{(s,2)} = 0$ (P) and $\lambda_{(s,1)} = 0$ (MM), a grey marker denotes the codimension-two point. The visualisations of blue and red surfaces in the isometric views represent the respective positive and negative isocontour values of the perturbative axial velocity indicated in the figure.

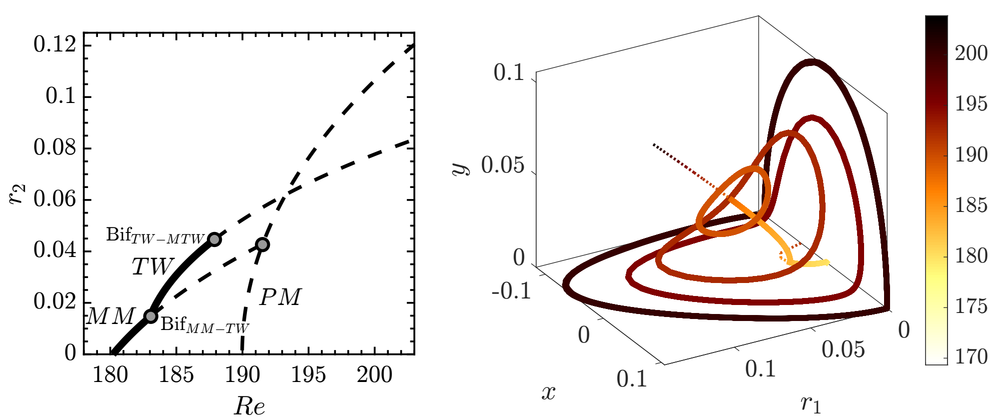

Figure 22: Bifurcation diagram with respect to the Reynolds number for $L = 1.15$ and $\delta_u = 0.8$. The left diagram reports the evolution of r_2 for the fixed point solutions of the normal form. The right diagram displays the bifurcation diagram in the Cartesian coordinates. Solid lines and dashed lines denote stable attractors and unstable attractors, respectively.

$m = 2$, herein denoted as pure mode (P). A reconstruction of the perturbative component of the flow field of such a state is performed at the bottom right of fig. 21, which shows that the state P possesses two orthogonal planes of symmetry. Near the codimension two point, for values of the velocity ratio $\delta_u < 1.1$, the state P is only observable, that is non-linearly stable, within a small interval with respect to the Reynolds number. For larger values of the velocity ratio, the state P remains stable within the analysed interval of Reynolds numbers. For values of the velocity ratio $\delta_u < 1.0$, the bifurcation diagram is more complex. Figure 22 displays the bifurcation diagram of the fixed-point solutions of eq. (5.5) on the left diagram and the full set of solutions of the normal form in the right diagram. The axisymmetric steady-state first bifurcates towards a Mixed-Mode solution, which is the solution in the $y = 0$ plane for the right diagram of fig. 22. A solution with a non-symmetric wake has been reconstructed in fig. 21. The Mixed-Mode solution is only stable within a small interval of the Reynolds number. A secondary bifurcation, denoted Bif_{MM-TW}, gives raise to a slowly rotating wave of the wake. The TW and the MM solutions are identical at the bifurcation point. The phase speed is zero at the bifurcation, thus this is not a Hopf bifurcation. It corresponds to a *drift instability* that breaks the azimuthal symmetry, i.e. it starts to slowly drift. This unusual feature, that travelling waves bifurcate from a steady solution at a steady bifurcation, is a generic feature of the $1:2$ resonance. A reconstruction of the travelling wave solution is depicted on the top of fig. 21. It corresponds to the line with non-zero y component in the right diagram of fig. 22. The TW solution loses its stability in a tertiary bifurcation, denoted as Bif_{TW-MTW}. It conforms to a Hopf bifurcation of the TW solution, which gives birth to a quasi-periodic solution name Modulated Travelling Wave (MTW). A representation of this kind of solution in the Cartesian coordinates (r_1, x, y) is depicted on the right image of fig. 22.

Eventually, the Modulated Travelling Wave experiences a global bifurcation. That occurs when the periodic MTW solution, in the (r_1, x, y) coordinates, nearly intersects the invariant $r_1 = 0$ and $y = 0$ planes. The transition sequence is represented in the right image of fig. 22 in the Cartesian coordinates (r_1, x, y). The amplitude of the MTW limit cycle increases until the MTW arising at the tertiary bifurcation Bif_{TW-MTW} are destroyed by meeting a heteroclinic cycle at Bif_{MTW-Ht}. The locus of Bif_{MTW-Ht} is reported in fig. 21 and in good agreement with Armbruster *et al.* (1988). The conditions for the existence of the heteroclinic cycles are: $\lambda_{(s,1)} > 0$, $\lambda_{(s,2)} > 0$, $c_{22} < 0$. When σ_- becomes negative, the cycle is attracting and robust heteroclinic cycles are observed. It is destroyed when σ_+ becomes negative, in that case the pure modes are no longer saddles which breaks the heteroclinic connection. Figure 23 displays the instantaneous fluctuation field from a heteroclinic orbit connecting P and its conjugate solution P', which is obtained by a rotation of $\pi/2$, for parameter values $\mathrm{Re} = 200$ and $\delta_u = 0.8$. The dynamics of the cycle takes place in two phases. Figure 23 depicts the motion of the coherent structure associated to the heteroclinic cycle. Starting from the conjugated pure mode P', the cycle leaves the point (a), located in the vicinity of P', along the unstable eigenvector y, which is the stable direction of P. The first phase consists in a rapid rotation by $\pi/2$ of the wake, it corresponds to the sequence a-b-c-d-e displayed in fig. 23. Then it is followed by a slow approach following the direction y and departure from the pure mode state P along the direction r_1. The second phase consists in a rapid horizontal motion of the wake, which is an evolution from P to P' that takes place by the breaking of the reflectional symmetry with respect to the vertical axis; it constitutes the sequence e-f-g-h-i-a. Please note that equivalent motions are also possible. The first phase of rapid counter-clockwise rotation by $\pi/2$ can be performed in the opposite sense. It corresponds to a motion in the Cartesian coordinates along the plane r_1 along negative values of y. The sequence e-f-g-h-i-a can be replaced by a horizontal movement in the opposite sense, which adjusts to connect the plane $y = 0$ corresponding to negative values of r_1.

6. Discussion & Conclusions

The current study provides a complete description of the configuration consisting of two coaxial jets, broadly found in industrial processes, covering a wide range of applications such as noise reduction, mixing enhancement, or combustion control. The numerical procedure

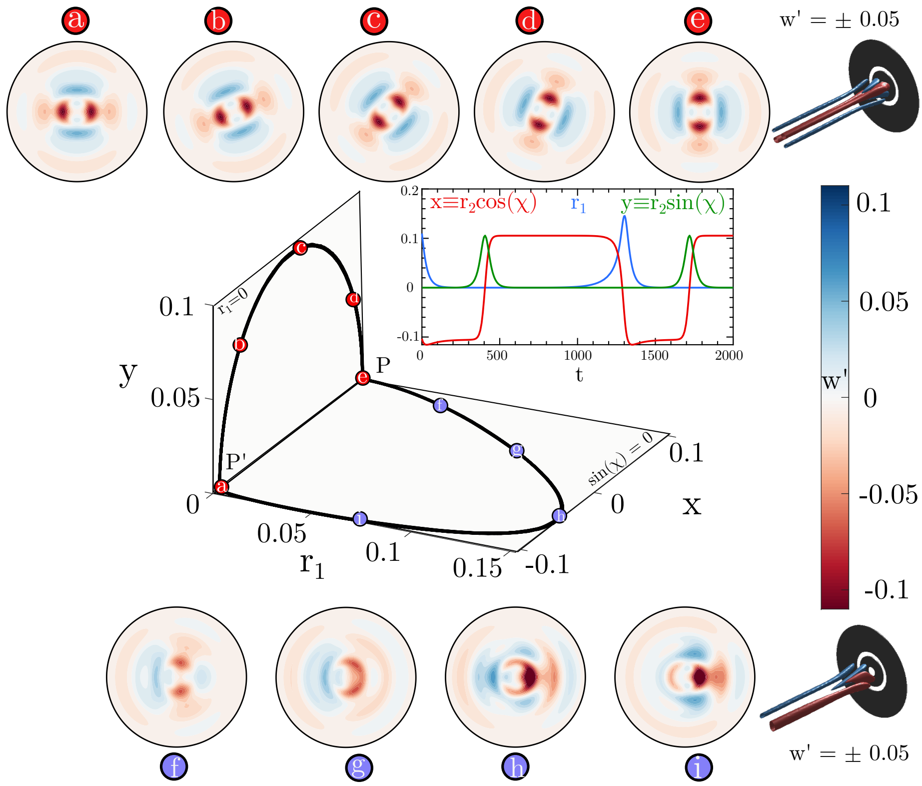

Figure 23: Heteroclinic cycle solution for parameter values Re = 200, $\delta_u = 0.8$. The top and bottom image sequences along the heteroclinic cycle show (from left to right) an axial slice plane at $z = 1$ of the instantaneous fluctuations of the axial velocity of the flow field as viewed from downstream, along with a three-dimensional isometric view (d on the top and g on the bottom).The middle diagram displays the heteroclinic cycle in the coordinates (r_1, x, y).

herein employed has been validated with the existing literature in the case of the stability analysis (see B for a detailed overview). A large region of the parameter space is explored $(\delta_u, L) \in ([0, 2], [0.5, 4.5])$, substantially expanding the work of Canton *et al.* (2017).

Section 3 provides an analysis of the basic properties of the steady-state, such as the topology of the flow and its variations in terms of the three parameters (Re, L, δ_u). It also highlights the existence of multiple steady-states, as a result of a series of saddle-node bifurcations, and its connection to the changes in the topology of the flow. Highlighting, nonetheless, that changes in the topology are not a direct consequence of a saddle-node bifurcation. The linear stability analysis performed in Section 4 reveals the existence of two unstable steady modes: S_1 and S_2, which are mostly located within the recirculation bubble, and two unsteady ones: F_1 and F_2, which are also produced within the recirculating region of the flow, but they are convected downstream, while experiencing substantial amplification. In addition, in section 4, we briefly discuss the consequences of the retraction and eventual disappearance of the recirculation bubble and the formation of a new recirculating flow region, aspects that have been covered in section 3, in terms of the sudden changes in the critical Reynolds number. Subsequently, the critical Reynolds number is determined for a wide range of inner-to-outer velocity rations and duct wall lengths. An increase of the velocity ratio has an overall stabilising effect, and it leads to the swap from mode S_1, characterised with one symmetry plane, to mode S_2 that possesses two symmetry planes. Afterwards, the effect of the distance L between jets is analysed. The primary effect of increasing this distance is a decrease in the critical Reynolds number for all values of δ_u investigated.

Section 5 analyses the mode interaction between two symmetry breaking modes with azimuthal wavenumbers $m = 1$ and $m = 2$. The unfolding of the codimension-two bifurcation reveals the presence of unsteadiness as a result of the resonant $1 : 2$ interaction between the two steady-modes. The codimension-two point is located at a velocity ratio $\delta_u = 1.0$ and distance between jets of $L = 1.15$, a situation that it is qualitatively equivalent to transitions found in the range $0.5 < \delta_u < 1.5$. For values lower than $\delta_u = 1.0$, the bifurcation diagram exhibits an intricate path. First, a Mixed-Mode (MM) solution emerges, which displays a non-symmetric wake. The Mixed-Mode solution is only stable for a small range of the Reynolds number. Subsequently, a slowly rotating wake is triggered in the form of a Travelling Wave (TW). This unusual feature, an unsteady state emerging from a steady state, corresponds to a drift instability commonly found at $1 : 2$ resonance. Then, the TW solution encounters a Hopf bifurcation, developing a quasi-periodic solution in the form of a Modulated Travelling Wave (MTW). Finally, the MTW solution undergoes a global bifurcation meeting a heteroclinic cycle (Ht). This heteroclinic orbit links the solution P with its conjugate solution P', spinning the wake from P' to P, and moving it horizontally from P to P'. On the other hand, for values higher than $\delta_u = 1.0$, a non-axisymmetric steady state emerges as a pure mode P with two orthogonal planes of symmetry. If the transition happens for values of the velocity ratio close to unity, a further increase in the velocity ratio rapidly leads to the heteroclinic cycle.
Physical realizations of the $1 : 2$ mode interaction have been observed by Mercader *et al.* (2002) and Nore *et al.* (2003, 2005) for confined flow configurations. However, to the author's knowledge, this is the first time that a robust heteroclinic cycle resulting from this type of $1 : 2$ interaction is reported in the literature for an external flow configuration, as it is the coaxial jet configuration.

A.C., J.A.M. and S.L.C. acknowledge the grant PID2020-114173RB-I00 funded by MCIN/AEI/ 10.13039/501100011033. S.L.C., J.A.M. and A.C. acknowledge the support of Comunidad de Madrid through the call Research Grants for Young Investigators from Universidad Politécnica de Madrid. AC also acknowledges the support of Universidad Politécnica de Madrid, under the programme 'Programa Propio'.

Appendix A. Normal form reduction

In this section we provide a detailed explanation of the normal form reduction to obtain the coefficients of eq. (2.11), we define the terms of the compact notation of the governing equations eq. (2.3), which is reminded here, for the sake of conciseness,

$$\mathbf{B}\frac{\partial \mathbf{Q}}{\partial t} = \mathbf{F}(\mathbf{Q},\boldsymbol{\eta}) \equiv \mathbf{L}\mathbf{Q} + \mathbf{N}(\mathbf{Q},\mathbf{Q}) + \mathbf{G}(\mathbf{Q},\boldsymbol{\eta}). \tag{A 1}$$

The nonlinear convective operator $\mathbf{N}(\mathbf{Q}_1,\mathbf{Q}_2) = \mathbf{U}_1\cdot\nabla\mathbf{U}_2$ accounts for the quadratic interaction on the state variable. The linear operator on the state variable is $\mathbf{L}\mathbf{Q} = [\nabla P, \nabla\cdot\mathbf{U}]^T$. The remaining term accounts for the linear variations in the state variable and the parameter vector. It is defined as $\mathbf{G}(\mathbf{Q},\boldsymbol{\eta}) = \mathbf{G}(\mathbf{Q},[\eta_1,0]^T) + \mathbf{G}(\mathbf{Q},[0,\eta_2]^T)$ where $\mathbf{G}(\mathbf{Q},[\eta_1,0]^T) = \eta_1\nabla\cdot(\nabla\mathbf{U}+\nabla\mathbf{U}^T)$ and $\mathbf{G}(\mathbf{Q},[0,\eta_2]^T)$. The former operator shows the dependency on the parameter η_1, which accounts for the viscous effects. The latter operator depends on the parameter η_2, which accounts for the velocity ratio between jets and it is used to impose the boundary condition $\mathbf{U} = (0, \eta_2 \tanh\big(b_i(1-2r)\big), 0)$ on $\Gamma_{in,i}$. In addition, we consider the following splitting of the parameters $\boldsymbol{\eta} = \boldsymbol{\eta}_c + \Delta\boldsymbol{\eta}$. Here $\boldsymbol{\eta}_c$ denotes the critical parameters $\boldsymbol{\eta}_c \equiv [Re_c^{-1}, \delta_{u,c}]^T$ attained when the spectra of the Jacobian operator possess at least an eigenvalue whose real part is zero. The distance in the parameter space to the threshold is represented by $\Delta\boldsymbol{\eta} = [Re_c^{-1} - Re^{-1}, \delta_{u,c} - \delta_u]^T$.

A.1. *Multiple scales ansatz*

The multiple scales expansion of the solution $\mathbf{q}$ of eq. (2.3) is

$$\mathbf{q}(t,\tau) = \mathbf{Q}_0 + \varepsilon\mathbf{q}_{(\varepsilon)}(t,\tau) + \varepsilon^2\mathbf{q}_{(\varepsilon^2)}(t,\tau) + O(\varepsilon^3), \tag{A 2}$$

where $\varepsilon \ll 1$ is a small parameter. The distance in the parameter space to the critical point $\Delta\boldsymbol{\eta} = [Re_c^{-1} - Re^{-1}, \delta_{u,c} - \delta_u]^T$ is assumed to be of second order, i.e. $\Delta\eta_i = O(\varepsilon^2)$ for $i = 1, 2$. The expansion eq. (A 2) considers a two scale expansion of the original time $t \mapsto t + \varepsilon^2\tau$. A fast timescale t and a slow timescale of the evolution of the amplitudes $z_i(\tau)$ in eq. (A 2), for $i = 1, 2$. Note that the expansion of the LHS eq. (2.3) up to third order is as follows

$$\varepsilon\mathbf{B}\frac{\partial \mathbf{q}_{(\varepsilon)}}{\partial t} + \varepsilon^2\mathbf{B}\frac{\partial \mathbf{q}_{(\varepsilon^2)}}{\partial t} + \varepsilon^3\Big[\mathbf{B}\frac{\partial \mathbf{q}_{(\varepsilon^3)}}{\partial t} + \mathbf{B}\frac{\partial \mathbf{q}_{(\varepsilon)}}{\partial \tau}\Big], \tag{A 3}$$

and the RHS respectively,

$$\mathbf{F}(\mathbf{q},\boldsymbol{\eta}) = \mathbf{F}_{(0)} + \varepsilon\mathbf{F}_{(\varepsilon)} + \varepsilon^2\mathbf{F}_{(\varepsilon^2)} + \varepsilon^3\mathbf{F}_{(\varepsilon^3)}. \tag{A 4}$$

The expansion eq. (A 4) will be detailed at each order.

A.1.1. *Order ε^0*

The zeroth order $\mathbf{Q}_0$ of the multiple scales expansion eq. (A 2) is the steady state of the governing equations evaluated at the threshold of instability, i.e. $\boldsymbol{\eta} = \boldsymbol{\eta}_c$,

$$\mathbf{0} = \mathbf{F}(\mathbf{Q}_0,\boldsymbol{\eta}_c). \tag{A 5}$$

A.1.2. *Order* ε^1

The first order $\mathbf{q}_{(\varepsilon)}(t,\tau)$ of the multiple scales expansion of eq. (A 2) is composed of the eigenmodes of the linearised system

$$\mathbf{q}_{(\varepsilon)}(t,\tau) \equiv \left(z_1(\tau)e^{-\mathrm{i}m_1\theta}\hat{\mathbf{q}}_1 + z_2(\tau)e^{\mathrm{i}-m_2\theta}\hat{\mathbf{q}}_2 + \text{c. c.}\right). \tag{A 6}$$

in our case, $m_1 = 1$ and $m_2 = 2$. Each term $\hat{\mathbf{q}}_\ell$ of the first order expansion eq. (A 6) is a solution of the following linear equation

$$\mathbf{J}_{(\omega_\ell,m_\ell)}\hat{\mathbf{q}}_\ell \equiv \left(i\omega_\ell\mathbf{B} - \frac{\partial\mathbf{F}}{\partial\mathbf{q}}|_{\mathbf{q}=\mathbf{Q}_0,\eta=\eta_c}\right)\hat{\mathbf{q}}_\ell = 0, \tag{A 7}$$

where $\frac{\partial\mathbf{F}}{\partial\mathbf{q}}|_{\mathbf{q}=\mathbf{Q}_0,\eta=\eta_c}\hat{\mathbf{q}}_\ell = \mathbf{L}_{m_\ell}\hat{\mathbf{q}}_\ell + \mathbf{N}_{m_\ell}(\mathbf{Q}_0,\hat{\mathbf{q}}_\ell) + \mathbf{N}_{m_\ell}(\hat{\mathbf{q}}_\ell,\mathbf{Q}_0)$. The subscript m_ℓ indicates the azimuthal wavenumber used for the evaluation of the operator.

A.1.3. *Order* ε^2

The second order expansion term $\mathbf{q}_{(\varepsilon^2)}(t,\tau)$ is determined from the resolution of a set of forced linear systems, where the forcing terms are evaluated from first and zeroth order terms. The expansion in terms of amplitudes $z_i(\tau)$ $(i = 1, 2)$ of $\mathbf{q}_{(\varepsilon^2)}(t,\tau)$ is assessed from term-by-term identification of the forcing terms at the second order. Non-linear second order terms in ε are

$$\begin{aligned}\mathbf{F}_{(\varepsilon^2)} &\equiv \sum_{j,k=1}^{2}\left(z_j z_k\mathbf{N}(\hat{\mathbf{q}}_j,\hat{\mathbf{q}}_k)e^{-\mathrm{i}(m_j+m_k)\theta} + \text{ c.c.}\right)\\ &+\sum_{j,k=1}^{2}\left(z_j\overline{z}_k\mathbf{N}(\hat{\mathbf{q}}_j,\overline{\hat{\mathbf{q}}}_k)e^{-\mathrm{i}(m_j-m_k)\theta} + \text{ c.c.}\right)\\ &+\sum_{\ell=0}^{2}\eta_\ell\mathbf{G}(\mathbf{Q}_0,\mathbf{e}_\ell),\end{aligned} \tag{A 8}$$

where the terms proportional to $z_j z_k$ are named $\hat{\mathbf{F}}^{(z_j z_k)}_{(\epsilon^2)}$ and $\mathbf{e}_\ell$ is an element of the orthonormal basis of $\mathbb{R}^2$.

Then, we look for a second order term expanded as follows

$$\mathbf{q}_{(\varepsilon^2)} \equiv \sum_{\substack{j,k=1\\ k\leqslant j}}^{2}\left(z_j z_k\hat{\mathbf{q}}_{z_j z_k} + z_j\overline{z}_k\hat{\mathbf{q}}_{z_j\overline{z}_k} + \text{ c.c }\right) + \sum_{\ell=1}^{2}\eta_\ell\mathbf{Q}_0^{(\eta_\ell)}. \tag{A 9}$$

Terms $\hat{\mathbf{q}}_{z_j^2}$ are azimuthal harmonics of the flow. The terms $\hat{\mathbf{q}}_{z_j z_k}$ with $j \neq k$ are coupling terms, and $\hat{\mathbf{q}}_{|z_j|^2}$ are harmonic base flow modification terms. Finally, $\mathbf{Q}_0^{(\eta_\ell)}$ are base flow corrections due to a variation of the parameter η_ℓ from the critical point.

At this order, there exist two resonant terms, the terms proportional to $\overline{z}_1 z_2$ and z_1^2, which are associated with the singular Jacobian $\mathbf{J}_{(0,m_k)}$ for $k = 1, 2$. To ensure the solvability of these terms, we must enforce compatibility conditions, i.e. the *Fredholm alternative*. The resonant terms are then determined from the resolution of the following set of *bordered systems*

$$\begin{pmatrix}\mathbf{J}_{(0,m_k)} & \hat{\mathbf{q}}_k\\ \hat{\mathbf{q}}_k^\dagger & 0\end{pmatrix}\begin{pmatrix}\hat{\mathbf{q}}_{(\mathbf{z}^{(R)})}\\ e\end{pmatrix} = \begin{pmatrix}\hat{\mathbf{F}}^{(\mathbf{z}^{(R)})}_{(\varepsilon^2)}\\ 0\end{pmatrix}, \quad \mathbf{z}^{(R)} \in [\overline{z}_1 z_2, z_1^2]^T, \tag{A 10}$$

where $e = e_3$ for $\mathbf{z}^{(R)} = \overline{z}_1 z_2$ and $e = e_4$ for $\mathbf{z}^{(R)} = z_1^2$. The non-resonant terms are computed by solving the following non-degenerated forced linear systems

$$\mathbf{J}_{(0,m_j+m_k)}\hat{\mathbf{q}}_{z_j z_k} = \hat{\mathbf{F}}^{(z_j z_k)}_{(\epsilon^2)}, \tag{A 11}$$

and

$$\mathbf{J}_{(0,0)}\mathbf{Q}_0^{(\eta_\ell)} = \mathbf{G}(\mathbf{Q}_0, \mathbf{e}_\ell). \tag{A 12}$$

A.1.4. *Order* ε^3

At third order, there exist six degenerate terms. In our case, we are not interested in solving for terms of third-order, instead, we will determine the linear and cubic coefficients of the third order normal form eq. (2.11) from a set of compatibility conditions.

The linear terms $\lambda_{(s,1)}$ and $\lambda_{s,2}$ and cubic terms $c_{(i,j)}$ for $i = 1, 2$ are determined as follows

$$\lambda_{(s,1)} = \frac{\langle \hat{\mathbf{q}}_1^\dagger, \hat{\mathbf{F}}^{(z_1)}_{(\varepsilon^3)} \rangle}{\langle \hat{\mathbf{q}}_z^\dagger, \mathbf{B}\hat{\mathbf{q}}_z \rangle}, \; \lambda_{(s,2)} = \frac{\langle \hat{\mathbf{q}}_2^\dagger, \hat{\mathbf{F}}^{(z_2)}_{(\varepsilon^3)} \rangle}{\langle \hat{\mathbf{q}}_2^\dagger, \mathbf{B}\hat{\mathbf{q}}_2 \rangle}, \; c_{(i,j)} = \frac{\langle \hat{\mathbf{q}}_2^\dagger, \hat{\mathbf{F}}^{(z_i|z_j|^2)}_{(\varepsilon^3)} \rangle}{\langle \hat{\mathbf{q}}_i^\dagger, \mathbf{B}\hat{\mathbf{q}}_i \rangle}. \tag{A 13}$$

The forcing terms for the linear coefficient are

$$\hat{\mathbf{F}}^{(z_j)}_{(\varepsilon^3)} \equiv \sum_{\ell=1}^{2} \eta_\ell \Big(\big[\mathbf{N}(\hat{\mathbf{q}}_j, \mathbf{Q}_0^{(\eta_\ell))} + \mathbf{N}(\mathbf{Q}_0^{(\eta_\ell)}, \hat{\mathbf{q}}_j) \big] + \mathbf{G}(\hat{\mathbf{q}}_j, \mathbf{e}_\ell) \Big). \tag{A 14}$$

which allows the decomposition of $\lambda_{(s,\ell)} = \lambda_{(s,\ell),\mathrm{Re}}(\mathrm{Re}_c^{-1}\mathrm{Re}^{-1}) + \lambda_{(s,\ell),\delta_u}(\delta_{u,c} - \delta_u)$ for $\ell = 1, 2$.

The forcing terms for the cubic coefficients are

$$\begin{aligned} \hat{\mathbf{F}}^{(z_j|z_k|^2)}_{(\varepsilon^3)} \equiv\; & \big[\mathbf{N}(\hat{\mathbf{q}}_j, \hat{\mathbf{q}}_{|z_k|^2}) + \mathbf{N}(\hat{\mathbf{q}}_{|z_k|^2}, \hat{\mathbf{q}}_j)\big] \\ & + \big[\mathbf{N}(\hat{\mathbf{q}}_{-k}, \hat{\mathbf{q}}_{z_j z_k}) + \mathbf{N}(\hat{\mathbf{q}}_{j,k}, \hat{\mathbf{q}}_{-k})\big] \\ & + \big[\mathbf{N}(\hat{\mathbf{q}}_k, \hat{\mathbf{q}}_{z_j \bar{z}_k}) + \mathbf{N}(\hat{\mathbf{q}}_{z_j \bar{z}_k}, \hat{\mathbf{q}}_k)\big]. \end{aligned} \tag{A 15}$$

if $j \neq k$ and

$$\begin{aligned} \hat{\mathbf{F}}^{(z_j|z_j|^2)}_{(\epsilon^3)} \equiv\; & \big[\mathbf{N}(\hat{\mathbf{q}}_j, \hat{\mathbf{q}}_{|z|_j^2}) + \mathbf{N}(\hat{\mathbf{q}}_{|z|_j^2}, \hat{\mathbf{q}}_j)\big] \\ & + \big[\mathbf{N}(\hat{\mathbf{q}}_{-j}, \hat{\mathbf{q}}_{z_j^2}) + \mathbf{N}(\hat{\mathbf{q}}_{z_j^2}, \hat{\mathbf{q}}_{-j})\big], \end{aligned} \tag{A 16}$$

for the diagonal forcing terms.

Appendix B. Validation of the code - Comparison with the literature

The calculations made in StabFem in the sections at the main manuscript are validated comparing the leading global mode in the geometry proposed by Canton *et al.* (2017). Moreover, the critical Reynolds number and associated frequency are also analysed. In the cited work, the authors use an analogous geometry with the following parameters:

- Radious of the inner jet $R_{inner} = 0.5$
- Diameter of the outer jet $D = 0.4$
- Distance between jets $L = 0.1$
- Ratio between velocities $\delta_u = 1$

The linear stability analysis has been carried out imposing $m = 0$, as done by Canton *et al.* (2017), so the leading global mode will be axisymmetric. The critical Reynolds number Re_c and the frequency ω of the leading global mode are compared in Tab. 3. As seen, few differences can be found on the critical Reynolds number and the frequency. The relative error in the Re_c calculation is 1.06% and the one of the frequency is 0.17%.

	Canton *et al.* (2017)	Present work
Re_c	1420	1405
ω	5.73	5.72

Table 3: Comparison of Re_c and ω between previous work and the present one.

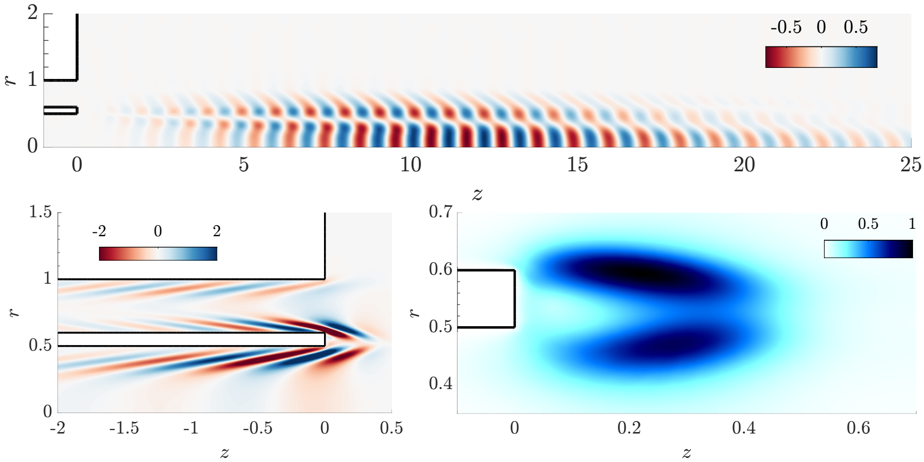

Figure 24: Direct mode, adjoint mode and sensitivity of the leading global mode studied by Canton *et al.* (2017) calculated using StabFem.

The global mode is now calculated using StabFem and compared with the one calculated by Canton *et al.* (2017). This mode can be found in figures 9, 10 and 11 on the cited paper. As it can be seen, there are not substantial differences between the direct modes, being both of them a vortex street with their biggest amplitude situated 10 units downstream the exit of the jets. The adjoint mode is concentrated within the nozzle, with its biggest amplitude situated on the sharp corners. There is no difference between the adjoint mode calculated with StabFem and the one in Canton *et al.* (2017). Finally, the structural sensitivity is similar to the one computed by Canton *et al.* (2017). It is composed by two lobes in the space between the exit of the two jets.

REFERENCES

Armbruster, Dieter, Guckenheimer, John & Holmes, Philip 1988 Heteroclinic cycles and modulated travelling waves in systems with o (2) symmetry. *Physica D: Nonlinear Phenomena* **29** (3), 257–282.

Auguste, F., Fabre, D. & Magnaudet, J. 2010 Bifurcations in the wake of a thick circular disk. *Theoretical and Computational Fluid Dynamics* **24**, 305–313.

Balestra, Gioele, Gloor, Michael & Kleiser, Leonhard 2015 Absolute and convective instabilities of heated coaxial jet flow. *Physics of Fluids* **27** (5).

Bogulawski, A. & Wawrzak, K. 2020 Absolute instability of an annular jet: local stability analysis. *Meccanica* **55**, 2179–2198.

Buresti, G., Talamelli, G. A. & Petagna, P. 1994 Experimental characterization of the velocity field of a coaxial jet configuration. *Exp. Therm. Fluid Sci.* **9**, 135.

Canton, J., Auteri, F. & Carini, M. 2017 Linear global stability of two incompressible coaxial jets. *J. Fluid Mech.* **824**, 886–911.

Dahm, W. J. A., Frieler, C. E. & Tryggvason, G. 1992 Vortex structure and dynamics in the near field of a coaxial jet. *J. Fluid Mech.* **241**, 371.

Dangelmayr, Gerhard 1986 Steady-state mode interactions in the presence of 0 (2)-symmetry. *Dynamics and Stability of Systems* **1** (2), 159–185.

Fabre, D., Citro, V., Ferreira Sabino, D., Bonnefis, P., Sierra, J., Giannetti, F. & Pigou, M. 2019 A Practical Review on Linear and Nonlinear Global Approaches to Flow Instabilities. *Applied Mechanics Reviews* **70** (6), 060802, arXiv: https://asmedigitalcollection.asme.org/appliedmechanicsreviews/article-pdf/70/6/060802/6075557/amr_070_06_060802.pdf.

Gianneti, F. & Luchini, P. 2007 Structural sensitivity of the first instability of the cylinder wake. *J. Fluid Mech.* **581**, 167–197.

Gloor, Michael, Obrist, Dominik & Kleiser, Leonhard 2013 Linear stability and acoustic characteristics of compressible, viscous, subsonic coaxial jet flow. *Physics of Fluids* **25** (8).

Jones, CA & Proctor, MRE 1987 Strong spatial resonance and travelling waves in bénard convection. *Physics Letters A* **121** (5), 224–228.

Kapitula, Todd & Promislow, Keith 2013 *Spectral and dynamical stability of nonlinear waves*, , vol. 457. Springer.

Ko, N.W.M. & Kwan, A.S.H. 1976 The initial region of subsonic coaxial jets. *J. Fluid Mech.* **73**, 305.

Mariano, Paolo Maria & Stazi, Furio Lorenzo 2005 Computational aspects of the mechanics of complex materials. *Archives of Computational Methods in Engineering* **12** (4), 391–478.

Meliga, Philippe, Chomaz, Jean-Marc & Sipp, Denis 2009 Global mode interaction and pattern selection in the wake of a disk: a weakly nonlinear expansion. *Journal of Fluid Mechanics* **633**, 159–189.

Meliga, Philippe, Gallaire, François & Chomaz, Jean-Marc 2012 A weakly nonlinear mechanism for mode selection in swirling jets. *Journal of Fluid Mechanics* **699**, 216–262.

Mercader, Isabel, Prat, Joana & Knobloch, Edgar 2002 Robust heteroclinic cycles in two-dimensional rayleigh–bénard convection without boussinesq symmetry. *International Journal of Bifurcation and Chaos* **12** (11), 2501–2522.

Michalke, A. 1999 Absolute inviscid instability of a ring jet with back-flow and swirl. *Eur. J. Mech. B/Fluids* **18**, 3–12.

Montagnani, Davide & Auteri, Franco 2019 Non-modal analysis of coaxial jets. *Journal of Fluid Mechanics* **872**, 665–696.

Nore, C, Moisy, F & Quartier, L 2005 Experimental observation of near-heteroclinic cycles in the von kármán swirling flow. *Physics of Fluids* **17** (6), 064103.

Nore, Caroline, Tuckerman, Laurette S, Daube, Olivier & Xin, Shihe 2003 The 1 [ratio] 2 mode interaction in exactly counter-rotating von kármán swirling flow. *Journal of Fluid Mechanics* **477**, 51–88.

Olsen, W. & Karchmer, A. 1976 Lip noise generated by flow separation from nozzle surfaces. *AIAA J.* **76**, 3.

Örlü, R., Segalini, A., Alfredsson, P. H. & Talamelli, A. 2008 On the passive control of the near-field of coaxial jets by means of vortex shedding. *Proceedings of the International Conference on Jets, Wakes and Separated Flows, ICJWSF-2008, Technical University of Berlin, Berlin, Germany, Sept. 16–19* .

Palacios, Antonio, Gunaratne, Gemunu H, Gorman, Michael & Robbins, Kay A 1997 Cellular pattern formation in circular domains. *Chaos: An Interdisciplinary Journal of Nonlinear Science* **7** (3), 463–475.

Perrault-Joncas, Dominique & Maslowe, Sherwin A. 2008 Linear stability of a compressible coaxial jet with continuous velocity and temperature profiles. *Physics of Fluids* **20** (7).

Porter, J & Knobloch, E 2001 New type of complex dynamics in the 1: 2 spatial resonance. *Physica D: Nonlinear Phenomena* **159** (3-4), 125–154.

Porter, J & Knobloch, E 2005 Dynamics in the 1: 2 spatial resonance with broken reflection symmetry. *Physica D: Nonlinear Phenomena* **201** (3-4), 318–344.

Rehab, H., Villermaux, E. & Hopfinger, E. J. 1997 Flow regimes of largevelocity-ratio coaxial jets. *J. Fluid Mech.* **345**, 357.

Segalini, A. & Talamelli, A. 2011 Experimental analysis of dominant instabilities in coaxial jets. *Phys. Fluids* **23**, 024103.

Sierra, Javier, Fabre, David & Citro, Vincenzo 2020*a* Efficient stability analysis of fluid flows using complex mapping techniques. *Computer Physics Communications* **251**, 107100.

Sierra, J., Fabre, D., Citro, V. & Giannetti, F. 2020*b* Bifurcation scenario in the two-dimensional laminar flow past a rotating cylinder. *Journal of Fluid Mechanics* **905**, A2.

SIERRA, J., JOLIVET, P., GIANNETTI, F. & CITRO, V. 2021 Adjoint-based sensitivity analysis of periodic orbits by the fourier–galerkin method. *Journal of Computational Physics* **440**, 110403.

SIERRA-AUSIN, JAVIER, CITRO, VINCENZO, GIANNETTI, FLAVIO & FABRE, DAVID 2022*a* Efficient computation of time-periodic compressible flows with spectral techniques. *Computer Methods in Applied Mechanics and Engineering* **393**, 114736.

SIERRA-AUSIN, J, FABRE, D, CITRO, V & GIANNETTI, F 2022*b* Acoustic instability prediction of the flow through a circular aperture in a thick plate via an impedance criterion. *Journal of Fluid Mechanics* **943**, A48.

SIERRA-AUSÍN, J., LORITE-DÍEZ, M., JIMÉNEZ-GONZÁLEZ, J.I., CITRO, V. & FABRE, D. 2022 Unveiling the competitive role of global modes in the pattern formation of rotating sphere flows. *Journal of Fluid Mechanics* **942**, A54.

DA SILVA, C. B., BALARAC, G. & MÉTAIS, O. 2003 Transition in high velocity ratio coaxial jets analysed from direct numerical simulations. *J. Turbul.* **24**, 1.

TALAMELLI, A. & GAVARINI, I. 2006 Linear instability characteristics of incompressible coaxial jets. *Flow Turbulence Combust.* **76**, 221–240.

TAMMISOLA, O. 2012 Oscillatory sensitivity patterns for global modes in wakes. *J. Fluid Mech.* **701**, 251–277.

WALLACE, D. & REDEKOPP, L.G. 1992 Linear instability characteristics of wake-shear layers. *Phys. Fluids* **4**, 189—-191.

WILLIAMS, T.J., ALI, M.R.M.H. & ANDERSON, J.S. 1969 Noise and flow characteristics of coaxial jets. *J. Mech. Eng. Sci.* **1**, 2.